

Implementation of disequilibrium chemistry to spectral retrieval code ARCiS and application to sixteen exoplanet transmission spectra

Indication of disequilibrium chemistry for HD 209458b and WASP-39b

Yui Kawashima^{1,2} and Michiel Min²

¹ Cluster for Pioneering Research, RIKEN, 2-1 Hirosawa, Wako, Saitama 351-0198, Japan

e-mail: yui.kawashima@riken.jp

² SRON Netherlands Institute for Space Research, Sorbonnelaan 2, 3584 CA Utrecht, The Netherlands

Received September 15, 1996; accepted March 16, 1997

ABSTRACT

Context. The retrieval approach is currently a standard method for deriving atmospheric properties from observed spectra of exoplanets. However, the approach ignores disequilibrium chemistry in most current retrieval codes, which can lead to misinterpretation of the metallicity or elemental abundance ratios of the atmosphere.

Aims. We have implemented the disequilibrium effect of vertical mixing or quenching for the major species in hydrogen/helium-dominated atmospheres, namely CH₄, CO, H₂O, NH₃, N₂, and CO₂, for the spectral retrieval code ARCiS with a physical basis.

Methods. We used the chemical relaxation method and developed a module to compute the profiles of molecular abundances taking the disequilibrium effect into account. Then, using ARCiS updated with this module, we have performed retrievals of the observed transmission spectra of 16 exoplanets with sizes ranging from Jupiter to mini-Neptune.

Results. We find indications of disequilibrium chemistry for HD 209458b ($\geq 4.1\sigma$) and WASP-39b ($\geq 2.7\sigma$). The retrieved spectrum of HD 209458b exhibits a strong NH₃ absorption feature at 10.5 μm accessible by JWST owing to an enhanced abundance of NH₃ due to the quenching effect. This feature is absent in the spectrum retrieved assuming equilibrium chemistry, which makes HD 209458b an ideal target for studying disequilibrium chemistry in exoplanet atmospheres. Moreover, for HAT-P-11b and GJ 436b, we obtain relatively different results than for the retrieval with the equilibrium assumption, such as a 2.9 σ difference for the C/O ratio. We have also examined the retrieved eddy diffusion coefficient, but could not identify a trend over the equilibrium temperature, possibly due to the limits of the current observational precision.

Conclusions. We have demonstrated that the assumption of equilibrium chemistry can lead to a misinterpretation of the observed data, showing that spectral retrieval with a consideration of disequilibrium chemistry is essential in the era of JWST and Ariel.

Key words. Planets and satellites: gaseous planets – Planets and satellites: atmospheres – Planets and satellites: composition

1. Introduction

Since the first discovery of an exoplanet in 1995 (Mayor & Queloz 1995), atmospheric spectra have been observed for dozens of exoplanets via transmission, emission, and direct imaging spectroscopy by both space- and ground-based telescopes. From these spectra, the abundances of several chemical species have been determined for some of the observed planets, most of which are expected to be abundant in hydrogen/helium-dominated atmospheres such as H₂O, CH₄, CO, and CO₂ (e.g., Line et al. 2014).

Recently, spectral retrieval models have come to be used as a standard when deriving the atmospheric properties from observed spectra (e.g., Irwin et al. 2008; Benneke & Seager 2012; Line et al. 2013; Waldmann et al. 2015; Fisher & Heng 2018; Mollière et al. 2019; Min et al. 2020). Since the computational cost of the spectral retrieval codes is quite high, some assumptions and/or simplifications have to be made for atmospheric chemistry. For simplicity, most of the current spectral retrieval models assume constant abundances of chemical species

throughout the atmosphere or their chemical equilibrium abundances, ignoring any disequilibrium chemistry.

In reality, however, the abundances of chemical species in the atmospheres cannot always be determined from the equilibrium chemistry, as has been studied by various 1D (photo-)chemical models (e.g., Kasting et al. 1985; Moses et al. 2011; Venot et al. 2012; Hu et al. 2012; Grassi et al. 2014; Rimmer & Helling 2016; Tsai et al. 2017; Kawashima & Ikoma 2018) and 2D or 3D atmospheric circulation models with chemistry (e.g., Cooper & Showman 2006; Agúndez et al. 2012, 2014; Drummond et al. 2018b,a; Mendonça et al. 2018; Drummond et al. 2020). Among the chemical disequilibrium processes such as photochemistry, the vertical quenching effect due to eddy diffusion transport is regarded as one of the most important because it significantly affects the atmospheric region where we can probe via observation. Indeed, Baxter et al. (2021) recently analyzed the transit depths of 49 gas giants measured at the 3.6 and 4.5 μm bands of *Spitzer* and found evidence of disequilibrium chemistry, which can be explained by the quenching effect of CH₄. Quenching happens at altitudes where the thermochem-

ical reaction timescale τ_{chem} is equal to that of the eddy diffusion τ_{diff} . Below this altitude, where $\tau_{\text{chem}} < \tau_{\text{diff}}$, the volume mixing ratio of a chemical species is consistent with that in thermochemical equilibrium due to high temperature and number density. On the other hand, above that altitude, where $\tau_{\text{diff}} < \tau_{\text{chem}}$, the abundance is “frozen” to the value at the quenching altitude since vertical transport due to eddy diffusion tends to smooth out the gradient of the volume mixing ratio. Thus, deriving the metallicity or elemental abundance ratios of the atmosphere from those frozen molecular abundances without considering the quenching effect can lead to over- or under-estimates of the metallicity or elemental abundance ratios. Because of the longer chemical timescale at lower temperatures, this quenching effect is especially important for cooler ($\lesssim 1000$ K) atmospheres, which are the primary targets for upcoming characterizations of exoplanet atmospheres.

Morley et al. (2017) introduced a quenching pressure as a parameter for spectral retrieval, assuming the same quenching pressures for all species. This treatment of the quenching effect was also adopted in Mollière et al. (2020). However, the quenching pressure should be different for each species because the chemical timescale is different for each species, especially between CH_4/CO and NH_3/N_2 (e.g., Moses 2014). Also, as a more general approach for capturing discontinuities in the abundance profiles, caused not only by vertical mixing but also by photodissociation and the formation of clouds and haze, Changeat et al. (2019) recently proposed a “two-layer” retrieval approach that allows the atmosphere to have different constant abundances in the upper and lower atmospheres.

Predicting the quenching pressure for each species with a physical basis involves calculating chemical reactions under the effect of eddy diffusion transport. It is, however, unrealistic to couple full kinetic chemistry to spectral retrieval codes even for 1D modeling due to its high computational cost. As such, we can refer to previous works that attempted to couple chemistry with computationally expensive 2D or 3D atmospheric circulation models to study the disequilibrium effect due to atmospheric circulation. Cooper & Showman (2006) adopted the chemical relaxation method, followed by further studies (e.g., Drummond et al. 2018b; Mendonça et al. 2018; Drummond et al. 2018a). The chemical relaxation scheme replaces numerous chemical production and loss terms in the continuity equation of a species with a single term given by the deviation of the abundance from the equilibrium value divided by its chemical timescale (Smith 1998; Cooper & Showman 2006). Other ways to reduce the computational cost have also been adopted, such as simplifying the atmospheric dynamics model (Agúndez et al. 2012, 2014) or using the reduced chemical network (Drummond et al. 2020).

When using the chemical relaxation method, adopting an appropriate chemical timescale for each species is important. The chemical timescale can be approximated by that of the rate-limiting or the slowest reaction along the conversion pathway from one species to another. Previous works have investigated the rate-limiting reaction for the conversion, such as that from CH_4 to CO and/or that from NH_3 to N_2 (e.g., Prinn & Barshay 1977; Yung et al. 1988; Visscher et al. 2010; Moses et al. 2011; Zahnle & Marley 2014). To revisit the chemical relaxation method, Tsai et al. (2018) derived the chemical timescales of the major species in hydrogen/helium-dominated atmospheres valid for the wide pressure and temperature ranges of currently observable exoplanet atmospheres, namely temperatures from 500 K to 3000 K and pressures from 0.1 mbar to 1000 bar.

In this paper, we adopt the chemical relaxation method to incorporate the effect of vertical mixing or quenching for each ma-

ior species in hydrogen/helium-dominated atmospheres into the spectral retrieval code ARCIS (Min et al. 2020) with a physical basis. This enables us to directly retrieve the eddy diffusion coefficient of exoplanet atmospheres, unlike for the various previous spectral retrieval codes. We note that we consider the quenching effect only as a disequilibrium process since this is what most affects the composition of the atmospheric region that we can probe by transmission spectroscopy in the optical and infrared. We neglect photochemistry, which is important in the upper atmosphere. We use the chemical timescales derived by Tsai et al. (2018) as they were validated for the broad pressure and temperature ranges important for exoplanet atmospheres. Then, using the updated ARCIS with the consideration of disequilibrium chemistry, we perform retrievals of the observed transmission spectra of exoplanets with sizes ranging from Jupiter to mini-Neptune and investigate the trend of disequilibrium chemistry in exoplanet atmospheres.

The rest of this paper is organized as follows. In Section 2, we describe our method and simulation setup. In Section 3, we present the results. In Section 4, we discuss several points that should be addressed in future works. Finally, we conclude this paper in Section 5.

2. Method

2.1. Model description

The one-dimensional continuity-transport equation for the number density of species i , n_i , is written as

$$\frac{\partial n_i}{\partial t} = P_i - L_i - \frac{\partial \Phi_i}{\partial z}, \quad (1)$$

where t and z are the time and altitude, respectively, P_i and L_i are the production and loss rates of n_i due to chemical reactions, respectively, and Φ_i is the vertical transport flux. Assuming that eddy diffusion is the dominant transport mechanism, which is usually the case for the atmospheric region of exoplanets that we can observe in the optical and infrared, Φ_i is given as

$$\Phi_i = -K_{zz}N \frac{\partial f_i}{\partial z}. \quad (2)$$

Here, K_{zz} is the eddy diffusion coefficient, which we assume to be constant throughout the atmosphere for simplicity, and N and f_i are the total number density of the gaseous species and the volume mixing ratio of species i , namely $f_i = n_i/N$, respectively.

The chemical relaxation method replaces the chemical source and sink terms of $P_i - L_i$ by the deviation from the equilibrium number density divided by the chemical timescale (Smith 1998; Cooper & Showman 2006). In that case, Eq. (1) can be rewritten as

$$\frac{\partial n_i}{\partial t} = -\frac{n_i - n_{i,\text{eq}}}{\tau_{i,\text{chem}}} - \frac{\partial \Phi_i}{\partial z}. \quad (3)$$

Here, $n_{i,\text{eq}}$ and $\tau_{i,\text{chem}}$ denote the equilibrium number density and chemical timescale of species i , respectively.

If we assume a steady-state condition, Eq. (3) can be further transformed as

$$n_i + \tau_{i,\text{chem}} \frac{\partial \Phi_i}{\partial z} = n_{i,\text{eq}}. \quad (4)$$

Next, we discretize Eq. (4) using the subscript j for the j th altitude layer, which we assume to have the same thickness of Δz as the other layers, as

$$n_{i,j} + \tau_{i,j,\text{chem}} \frac{\Phi_{i,j+\frac{1}{2}} - \Phi_{i,j-\frac{1}{2}}}{\Delta z} = n_{i,j,\text{eq}}. \quad (5)$$

Here, we approximate the diffusion fluxes at the boundary between the $j + 1$ th and j th layers and that between the j th and $j - 1$ th layers, $\Phi_{i,j+\frac{1}{2}}$ and $\Phi_{i,j-\frac{1}{2}}$, as

$$\Phi_{i,j+\frac{1}{2}} = -K_{zz}N_{j+\frac{1}{2}} \frac{f_{i,j+1} - f_{i,j}}{\Delta z} \quad (6)$$

and

$$\Phi_{i,j-\frac{1}{2}} = -K_{zz}N_{j-\frac{1}{2}} \frac{f_{i,j} - f_{i,j-1}}{\Delta z}. \quad (7)$$

$N_{j+\frac{1}{2}}$ and $N_{j-\frac{1}{2}}$ are the total number densities at those boundaries.

Finally, we can convert Eq. (5) into the matrix form as

$$(\mathbf{E} + \mathbf{T}_i \mathbf{M}_i) \mathbf{n}_i = \mathbf{n}_{i,\text{eq}}. \quad (8)$$

Here, \mathbf{E} is the identity matrix, and the other matrices are given as follows. \mathcal{N} is the number of the altitude layers and ‘‘diag’’ indicates a diagonal matrix.

$$\mathbf{n}_i = (n_{i,1}, n_{i,2}, n_{i,3}, \dots, n_{i,j}, \dots, n_{i,\mathcal{N}})^T \quad (9)$$

$$\mathbf{n}_{i,\text{eq}} = (n_{i,1,\text{eq}}, n_{i,2,\text{eq}}, n_{i,3,\text{eq}}, \dots, n_{i,j,\text{eq}}, \dots, n_{i,\mathcal{N},\text{eq}})^T \quad (10)$$

$$\mathbf{T}_i = \text{diag}(\tau_{i,1,\text{chem}}, \tau_{i,2,\text{chem}}, \tau_{i,3,\text{chem}}, \dots, \tau_{i,j,\text{chem}}, \dots, \tau_{i,\mathcal{N},\text{chem}}) \quad (11)$$

$$\mathbf{M}_i = -K_{zz} \begin{pmatrix} 0 & 0 & 0 & \dots & \dots & \dots & \dots & \dots & 0 \\ \frac{1}{\Delta z_2^2} \frac{N_{\frac{3}{2}}}{N_1} & -\frac{1}{\Delta z_2^2} \frac{N_{\frac{3}{2}} + N_{\frac{5}{2}}}{N_2} & \frac{1}{\Delta z_2^2} \frac{N_{\frac{5}{2}}}{N_3} & 0 & \dots & \dots & \dots & \dots & 0 \\ 0 & \frac{1}{\Delta z_3^2} \frac{N_{\frac{5}{2}}}{N_2} & -\frac{1}{\Delta z_3^2} \frac{N_{\frac{5}{2}} + N_{\frac{7}{2}}}{N_3} & \frac{1}{\Delta z_3^2} \frac{N_{\frac{7}{2}}}{N_4} & 0 & \dots & \dots & \dots & 0 \\ \vdots & \vdots & \vdots & \ddots & \vdots & \vdots & \vdots & \vdots & \vdots \\ 0 & \dots & 0 & \frac{1}{\Delta z_j^2} \frac{N_{j-\frac{1}{2}}}{N_{j-1}} & -\frac{1}{\Delta z_j^2} \frac{N_{j-\frac{1}{2}} + N_{j+\frac{1}{2}}}{N_j} & \frac{1}{\Delta z_j^2} \frac{N_{j+\frac{1}{2}}}{N_{j+1}} & 0 & \dots & 0 \\ \vdots & \vdots & \vdots & \vdots & \ddots & \ddots & \vdots & \vdots & \vdots \\ \vdots & \vdots & \vdots & \vdots & \vdots & \ddots & \ddots & \vdots & \vdots \\ 0 & \dots & \dots & \dots & \dots & \dots & 0 & \frac{1}{\Delta z_{\mathcal{N}}^2} \frac{N_{\mathcal{N}-\frac{1}{2}}}{N_{\mathcal{N}-1}} & -\frac{1}{\Delta z_{\mathcal{N}}^2} \frac{N_{\mathcal{N}-\frac{1}{2}}}{N_{\mathcal{N}}} \end{pmatrix} \quad (12)$$

In the above, we have adopted the lower boundary condition of the chemical equilibrium $n_{i,1} = n_{i,1,\text{eq}}$ because of the short chemical timescale in the deeper atmosphere. For the upper boundary condition, we have adopted zero flux, namely without atmospheric escape. By multiplying both sides of Eq. (8) by the inverse matrix of $(\mathbf{E} + \mathbf{T}_i \mathbf{M}_i)$, we finally get the solution as

$$\mathbf{n}_i = (\mathbf{E} + \mathbf{T}_i \mathbf{M}_i)^{-1} \mathbf{n}_{i,\text{eq}}. \quad (13)$$

We note that this equation leads to $n_i \sim n_{i,\text{eq}}$, namely in equilibrium, when K_{zz} has a negligible value.

2.2. Implementation to ARCiS

We have implemented this module to the spectral retrieval code ARCiS (ARtful modelling Code for exoplanet Science; Min et al. 2020) using the chemical timescales of CH_4 , CO , H_2O , NH_3 , and N_2 from Tsai et al. (2018). We note that for the chemical timescales of CH_4 , CO , and H_2O , their different expressions above and below the C/O ratio of unity are used. CO_2 tends to remain in pseudo-equilibrium even after its related molecules CO and H_2O are quenched (Moses et al. 2011; Tsai et al. 2018). Thus, for the calculation of CO_2 abundance, instead of using Eq. (13), we adopt the following pseudo-equilibrium abundance formula of Tsai et al. (2018),

$$n_{\text{CO}_2} = \frac{n_{\text{CO}} n_{\text{H}_2\text{O}}}{n_{\text{CO,eq}} n_{\text{H}_2\text{O,eq}}} n_{\text{CO}_2,\text{eq}}, \quad (14)$$

which modifies the CO_2 number density based on the quenched abundances of CO and H_2O when they are quenched. All the species except for the above are assumed to have their equilibrium abundances.

ARCiS uses GGchem (Woitke et al. 2018) for the calculation of thermochemical equilibrium abundances. The original version of GGchem did not include CH_2OH , CH_3OH , and N_2H_3 , the abundances of which are needed to calculate the chemical timescale of the species mentioned above. Taking their thermodynamic data from Burcat et al. (2005)¹, we have added these species to GGchem, available on the GitHub page of GGchem².

2.3. Application to the observed transmission spectra of 16 planets

With the updated ARCiS, we performed spectral retrievals where disequilibrium chemistry is allowed to affect the profiles of the molecular abundances (hereafter, ‘‘disequilibrium retrieval’’). To investigate the effect of the inclusion of disequilibrium chemistry to the retrieval code, we also performed retrievals imposing equilibrium chemistry (hereafter, ‘‘equilibrium retrieval’’) and compared the results of the two retrievals.

For the planet samples, we selected ten hot Jupiters and six Neptunes compiled in Sing et al. (2016) and Crossfield & Kreidberg (2017), respectively. High-precision transmission spectra

¹ <http://garfield.chem.elte.hu/Burcat/burcat.html>

² <https://github.com/pw31/GGchem>

Table 1: References for the observational data

Planet	Reference
GJ 436b	Knutson et al. (2011) ¹ Knutson et al. (2014) Morello et al. (2015) ² Lothringer et al. (2018)
GJ 1214b	Fraine et al. (2013) ³ Kreidberg et al. (2014) ⁴
GJ 3470b	Benneke et al. (2019)
HAT-P-1b*	Wakeford et al. (2013) Nikolov et al. (2014)
HAT-P-11b	Chachan et al. (2019)
HAT-P-12b	Wong et al. (2020)
HAT-P-26b	Wakeford et al. (2017)
HD 97658b	Guo et al. (2020) ⁵
HD 189733b*	Pont et al. (2013) McCullough et al. (2014) Sing et al. (2016)
HD 209458b*	Sing et al. (2016)
WASP-6b	Carter et al. (2020)
WASP-12b*	Sing et al. (2013) Kreidberg et al. (2015) Sing et al. (2016)
WASP-17b	Sing et al. (2016)
WASP-19b*	Huitson et al. (2013) Sing et al. (2016)
WASP-31b	Sing et al. (2015) Sing et al. (2016)
WASP-39b	Sing et al. (2016) Fischer et al. (2016) Wakeford et al. (2018)

* Planet samples with masses larger than half Jupiter mass, for which disequilibrium retrieval with fixed T_{int} is additionally performed.

¹ The average of three measurements at the *Spitzer* 8.0 μm band is used, excluding the observed transit on UT 2009 February 2 due to the possible stellar activity effect.

² The results presented in Table 6 are used.

³ The “simultaneous” fit results are used.

⁴ The “divide-white” fit results are used.

⁵ Following the approach of this study, we do not include the HST/STIS data points for our retrieval due to their large discrepancy at long wavelengths. Also, the results derived using the “logarithmic visit-long trend” are used.

were observed by the *Hubble* Space Telescope (HST) and *Spitzer* Space Telescope for those planets. The samples are listed in Table 1, along with the references for their observed transmission spectrum data used in the retrieval. These planet samples range from clear to cloudy atmospheres, and we note that the hot Jupiter samples and their spectral data are the same as those used in Min et al. (2020) except for HAT-P-12b, for which we adopt the observation data recently analyzed by Wong et al. (2020).

We adopt the same settings as the “constrained retrieval” of Min et al. (2020), which considered the thermal and cloud structures with the models of Guillot (2010) and Ormel & Min

(2019), respectively, and adopted the pre-computed opacities presented in Chubb et al. (2021). The retrieval parameters and the employed ranges and priors of those parameters are presented in Table 2. They are also the same as in Min et al. (2020), except for the eddy diffusion coefficient used in the disequilibrium chemistry module K_{zz}^{Ch} , which was not considered in the previous retrieval. In this study, as a first step to consider disequilibrium chemistry in spectral retrieval, we define a “standard” disequilibrium retrieval as a retrieval treating the eddy diffusion coefficient used in the chemistry calculation K_{zz}^{Ch} and that used in the cloud simulation K_{zz}^{Cl} independently. This is because the atmospheric region where clouds exist and the region where chemical species affecting the spectra are located are usually different, and hence the two eddy diffusion coefficients reflect the coefficients at different parts of the atmosphere. Moreover, we also examine the effect of imposing the condition that the two eddy diffusion coefficients are the same, namely $K_{zz}^{\text{Ch}} = K_{zz}^{\text{Cl}}$ (hereafter, “same- K_{zz} disequilibrium retrieval”). Retrieval with a non-constant coefficient along the altitude is left as a future work. We note that for the retrieval of WASP-12b, in the same way as Min et al. (2020), we adopt an additional parameter, which allows the scaling of the data from Kreidberg et al. (2015) to match the remaining data points due to the existing slight offset of their data when compared to the other data (Sing et al. 2013, 2016). See Min et al. (2020) for a detailed treatment of this additional parameter.

Our disequilibrium retrieval can also treat the equilibrium case since a negligible value of K_{zz} leads to the molecular abundances in equilibrium, as indicated in Eq. (13). We have confirmed that the lower bound of K_{zz}^{Ch} we adopted, namely $10^0 \text{ cm}^2 \text{ s}^{-1}$, is small enough to give molecular abundances consistent with the equilibrium values for the hotter planets of our samples. For some cooler planets, however, a few species deviate from their equilibrium abundances even for $K_{zz}^{\text{Ch}} = 10^0 \text{ cm}^2 \text{ s}^{-1}$. This is because the chemical timescale becomes exceedingly long at lower temperatures (see Figure 4 of Tsai et al. 2018). Considering a \sim Gyr planetary age timescale, $K_{zz}^{\text{Ch}} = 10^0 \text{ cm}^2 \text{ s}^{-1}$ is approximately the limit for the vertical transport by eddy diffusion to affect molecular abundances within the planetary age. Here, we estimate the diffusion timescale as $\tau_{\text{diff}} \sim H^2/K_{zz}$ using the atmospheric scale height H of each of our samples. Thus, we set the lower bound of K_{zz}^{Ch} to be $10^0 \text{ cm}^2 \text{ s}^{-1}$ even though the exploration range of K_{zz}^{Ch} does not include the “true” equilibrium regime for a few minor species in relatively cool planets such as GJ 436b, GJ 1214b, GJ 3470b, HAT-P-1b, HAT-P-11b, HAT-P-12b, HAT-P-26b, HD 97658b, HD 209458b, WASP-31b, and WASP-39b. We have estimated this using the best-fit parameter set that yields the minimum χ^2 compared to the observed data from our standard disequilibrium retrieval calculations for each of our samples.

Finally, in addition to the aforementioned two disequilibrium retrievals, we also conduct a disequilibrium retrieval fixing one of the highly uncertain parameters, namely the intrinsic temperature T_{int} , to an estimated value based on current knowledge. This is done based on the expectation that quenching often happens in the deeper atmosphere, especially for the nitrogen species, which means that the retrieval of K_{zz}^{Ch} can degenerate with T_{int} . We assume the value of T_{int} for each of our planet samples using its relation to the equilibrium temperature T_{eq} at a thermal equilibrium inferred by Thorngren et al. (2019), who derived the fraction ϵ of the incident flux on the planet F that heats the interior sufficiently to reproduce the observed radii of their hot Jupiter samples as a function of F . When assuming thermal equilibrium

Table 2: Retrieval parameters

Parameter	Symbol	Range	Unit	Prior
Ratio of the visible to infrared opacity	γ	10^{-2} – 10^2		flat log
Irradiation parameter	f_{irr}	0.00–0.25		flat linear
Infrared opacity	κ_{IR}	10^{-4} – 10^4	$\text{cm}^2 \text{g}^{-1}$	flat log
Intrinsic temperature ¹	T_{int}	10–3000	K	flat log
C/O ratio	C/O	0.1–1.3		flat linear
Si/O ratio	Si/O	0.0–0.3		flat linear
N/O ratio	N/O	0.0–0.3		flat linear
Metallicity	Z	–1–3	dex	flat linear
Reference radius at 10 bar pressure	R_{ref}	5σ around the literature planetary radius	Jupiter radius	flat linear
Planetary gravity	$\log_{10} g$	5σ around the literature value	cm s^{-2} for g	Gaussian
Diffusion coefficient for cloud ²	K_{zz}^{Cl}	10^5 – 10^{12}	$\text{cm}^2 \text{s}^{-1}$	flat log
Cloud nucleation rate	Σ	10^{-17} – 10^{-7}	$\text{g cm}^{-2} \text{s}^{-1}$	flat log
Diffusion coefficient for chemistry ³	K_{zz}^{Ch}	10^0 – 10^{15}	$\text{cm}^2 \text{s}^{-1}$	flat log

¹ Excluded for the disequilibrium retrieval with fixed T_{int}

² Not used in the same- K_{zz} retrieval. Instead, $K_{zz}^{\text{Cl}} = K_{zz}^{\text{Ch}}$ is assumed.

³ Used only for the disequilibrium retrievals

for the planet interiors, which will be reached in as little as tens of megayears, that fraction directly relates T_{eq} and T_{int} as (Thorngrén & Fortney 2018)

$$T_{\text{int}} = \epsilon (F)^{1/4} T_{\text{eq}} \sim 0.39 T_{\text{eq}} \exp\left(-\frac{(\log_{10} F - 0.14)^2}{1.095}\right), \quad (15)$$

where $F = 4\sigma T_{\text{eq}}^4$ in units of $\text{Gerg cm}^{-2} \text{s}^{-1}$ with the Stefan–Boltzmann constant σ . We adopt this assumption for this retrieval. Since their formula was inferred from planet samples with masses larger than half Jupiter mass (Thorngrén & Fortney 2018), we apply this type of disequilibrium retrieval only to the planets that satisfy this criterion, namely HAT-P-1b, HD 189733b, HD 209458b, WASP-12b, and WASP-19b. For those planets, the adopted values of T_{int} are 476, 376, 561, 517, and 653 K, respectively.

3. Results

3.1. Standard disequilibrium retrieval in comparison with equilibrium retrieval

In this section, we present the results of the standard disequilibrium retrieval and their differences from the equilibrium retrieval. As we have mentioned in § 2.3, for hotter planet samples, our disequilibrium retrieval can also treat the equilibrium cases. In Fig. 1, we show the results of the spectra from the standard disequilibrium and equilibrium retrievals along with those of the disequilibrium retrieval with the same K_{zz} and that with fixed T_{int} (only shown for the planets with masses larger than half Jupiter mass), which we discuss in § 3.2 and 3.3, respectively. Also, the retrieved pressure–temperature structure and the abundance profiles for four representative planets are shown in the left and right panels of Fig. 2, respectively. The profiles for the other planets are presented in Fig. A.1 of Appendix A. In addition, plots of the posterior distributions of the parameters from the sampling are presented in Fig. B.1 of Appendix B.

The second column of Table 3 presents the natural logs of the Bayes factors between the standard disequilibrium and equilibrium retrievals. It can be seen that except for HD 209458b, and tentatively GJ 3470b and WASP-39b, the differences are almost negligible (cf. Trotta 2008), which means that the retrieved

parameters from either of the two retrievals are barely favored over the parameters from the other retrieval. For HD 209458b and WASP-39b, the natural logs of the Bayes factors indicate that the disequilibrium scenario is favored over the equilibrium scenario by $\geq 4.1\sigma$ and $\geq 2.7\sigma$, respectively, calculated with Eq. (27) of Trotta (2008). For GJ 3470b, the value of the Bayes factor implies the preferability of the equilibrium scenario with $\geq 3.0\sigma$. However, as mentioned in § 2.3, for this planet, a few species still deviate from their equilibrium abundances even for the lower bound of the adopted K_{zz}^{Ch} range, namely $10^0 \text{ cm}^2 \text{ s}^{-1}$. Thus, it is uncertain whether the “true” equilibrium scenario is indeed favored. Retrieval simulation extending the lower bound of K_{zz}^{Ch} is needed to confirm this. For the retrieved spectra, thermal structures, abundance profiles, and parameters (see Figs. 1, 2, A.1, and B.1), HD 209458b and WASP-39b exhibit relatively large differences between the disequilibrium and equilibrium retrievals while they are largely similar within the uncertainty range for the other planets. This is consistent with the relatively large eddy diffusion coefficients retrieved for those two planets, such as $\log_{10}(K_{zz}^{\text{Ch}} [\text{cm}^2 \text{ s}^{-1}]) = 13.12^{+1.39}_{-4.61}$ for HD 209458b and $8.61^{+3.68}_{-4.22}$ for WASP-39b, inferring that disequilibrium chemistry is playing an essential role in their atmospheres.

For HD 209458b, while the retrieved spectra from both retrievals match relatively well in the wavelength range below $1.6 \mu\text{m}$ (see Fig. 1a), where precise observational data exists, differences are observed around 2.5–4.0, 6.5–9, and 9–13 μm . The discrepancies at the former two wavelength regions mainly come from the difference in the CH_4 abundance. A comparison of the pink thick solid line and pink thin solid line in Fig. 2(a) shows that the CH_4 abundance is quenched in the deeper atmosphere with a pressure around 1 bar, resulting in a smaller abundance compared to the equilibrium retrieval case (pink thick dashed line). While quenching reduces the CH_4 abundance in the observable pressure region, it works to maintain a high NH_3 abundance (compare yellow thick solid line and yellow thin solid line in Fig. 2a). This results in the prominent NH_3 absorption feature at $10.5 \mu\text{m}$ for the disequilibrium retrieval case (blue line in Fig. 1a), while that feature hardly exists in the equilibrium retrieval case (orange line).

To understand which observed features require the condition of disequilibrium chemistry for HD 209458b, we have additionally performed standard disequilibrium and equilib-

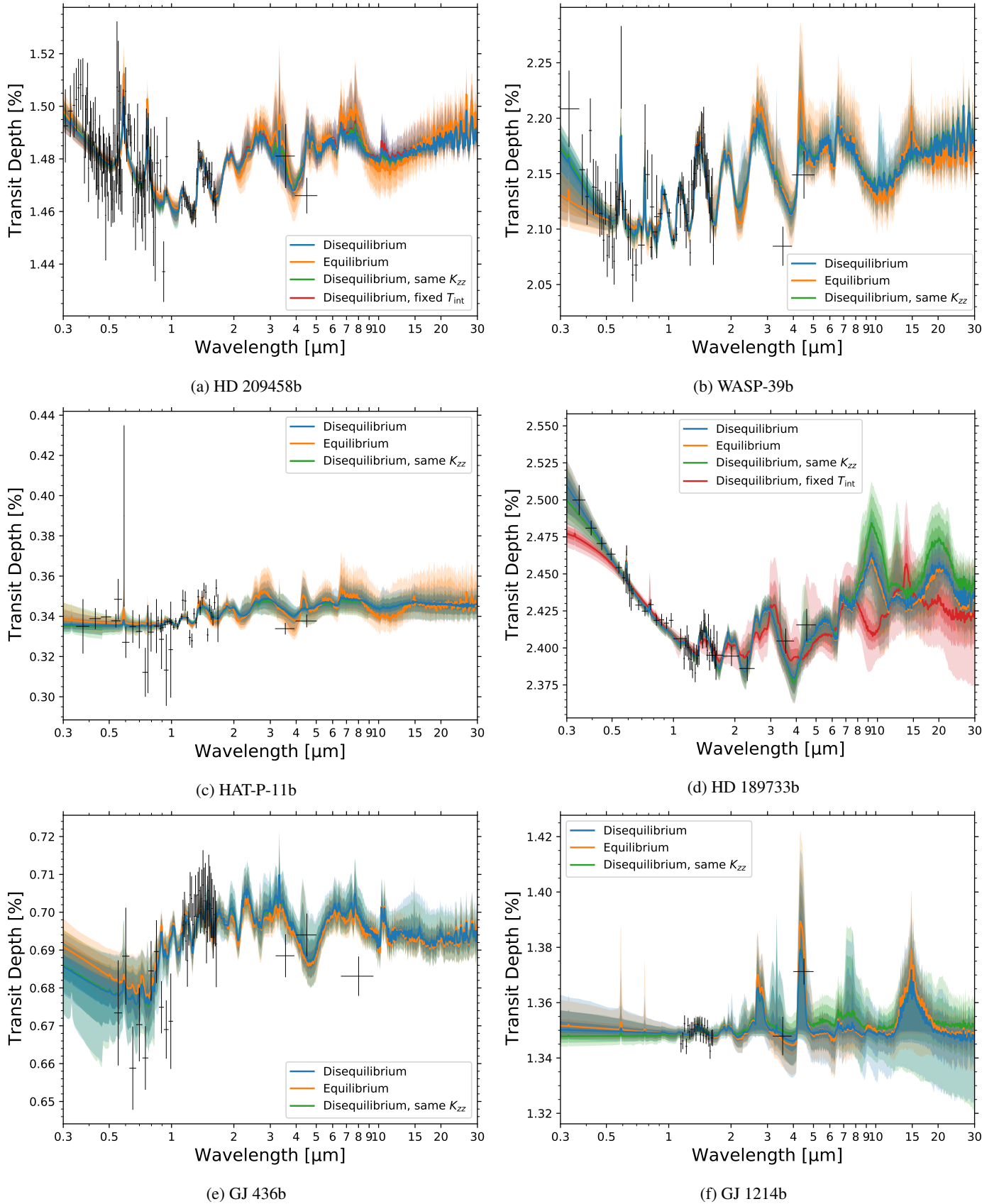
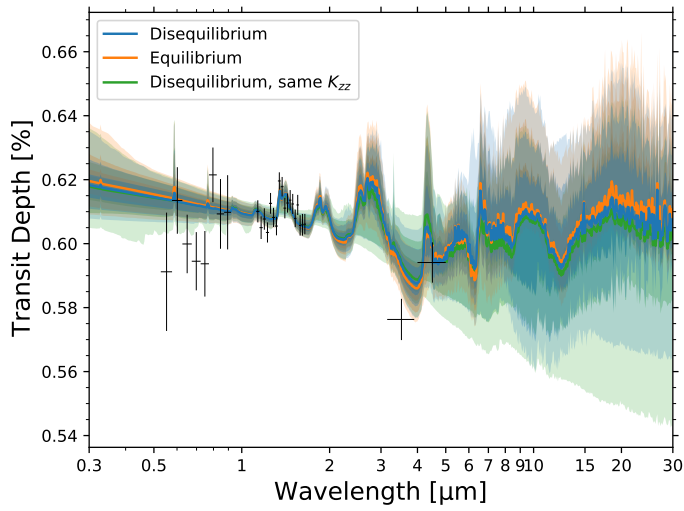
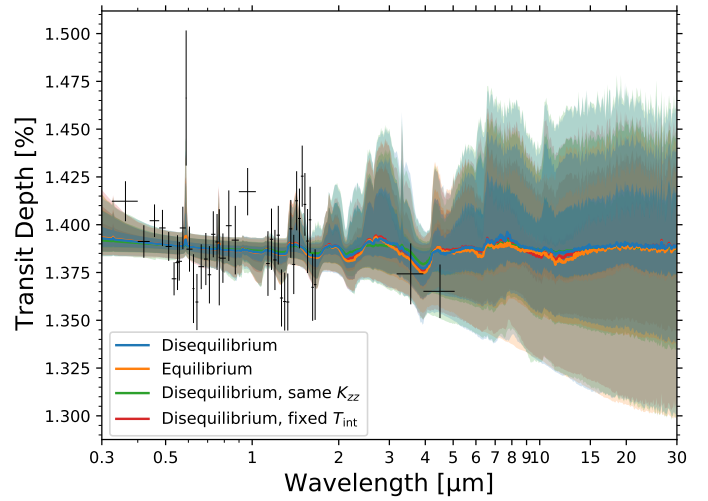


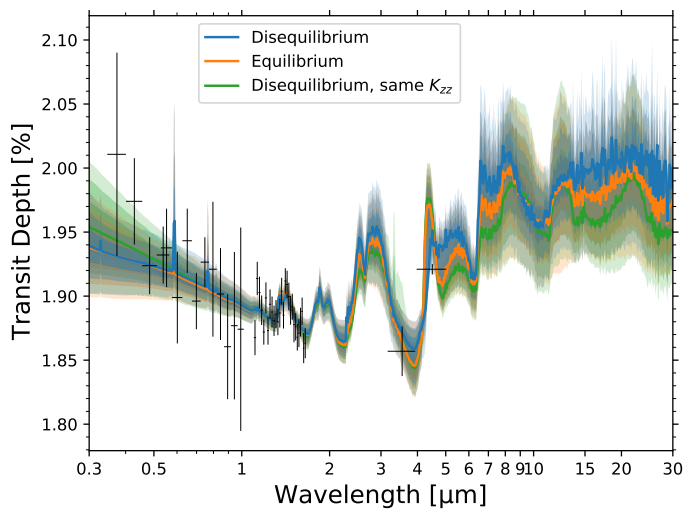
Fig. 1: Transmission spectra retrieved from the standard disequilibrium retrieval (blue), equilibrium retrieval (orange), and disequilibrium retrievals with the same K_{zz} (green) and with fixed T_{int} (red; only shown for planets with masses larger than half Jupiter mass). The solid lines show the median models while the shaded regions indicate the 1, 2, and 3σ confidence intervals. The black points denote the observed data used.



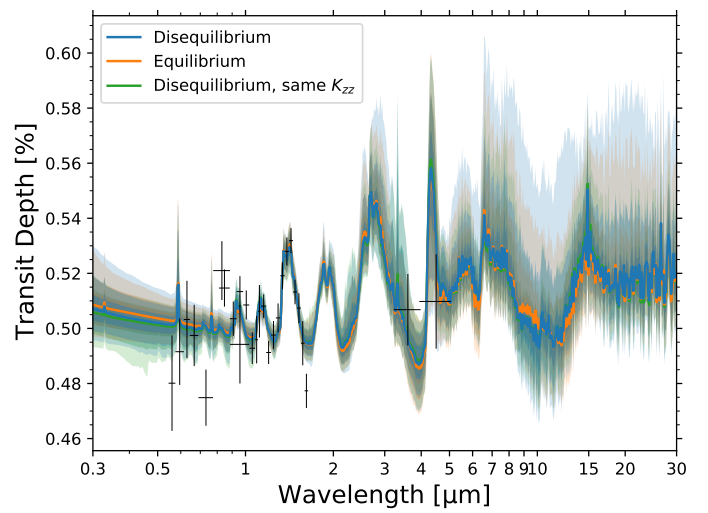
(g) GJ 3470b



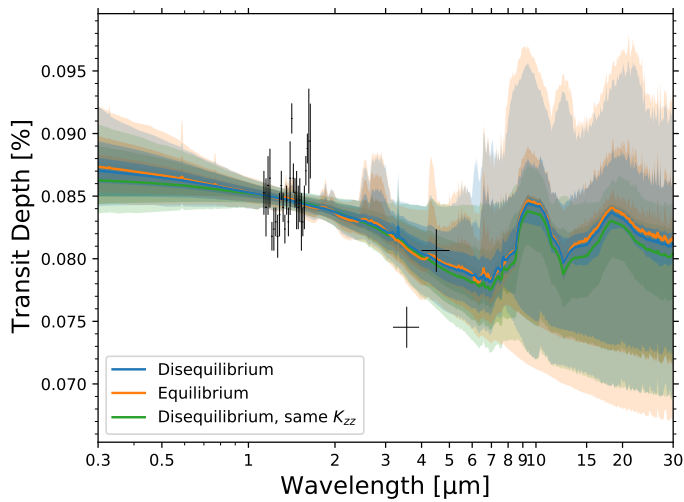
(h) HAT-P-1b



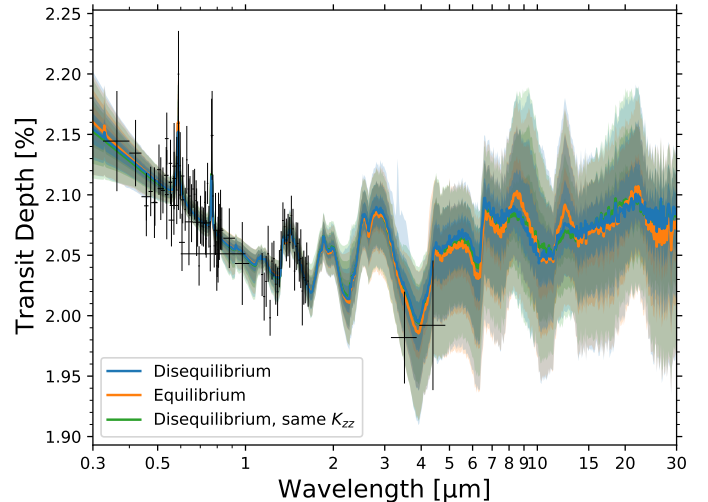
(i) HAT-P-12b



(j) HAT-P-26b



(k) HD 97658b



(l) WASP-6b

Fig. 1: Continued.

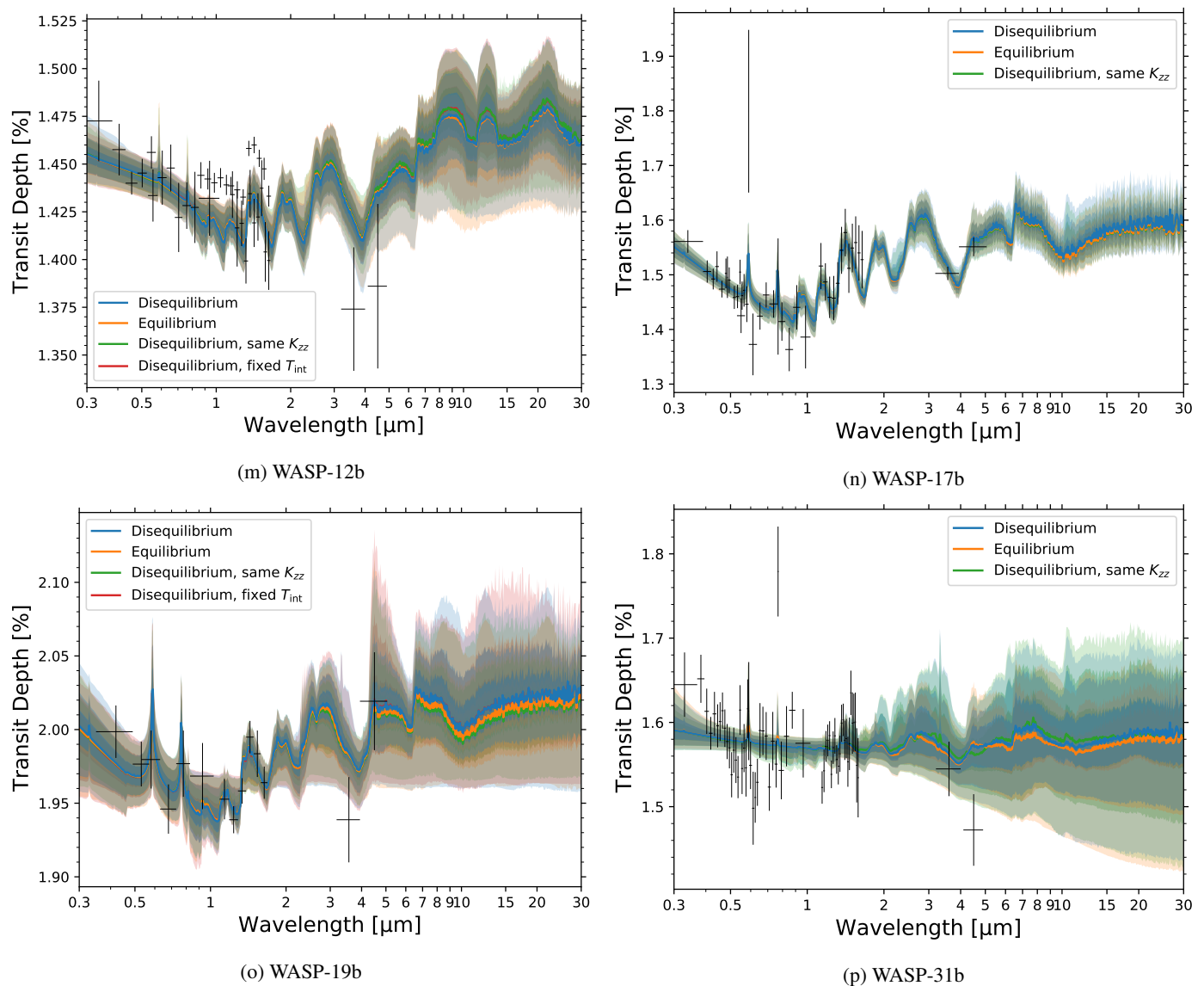


Fig. 1: Continued. Note that for (m) WASP-12b, even though the observed data of Kreidberg et al. (2015) are allowed to vertically shift in each retrieval simulation (see § 2.3 for details), their original values are plotted.

rium retrievals systematically excluding each observed data. Natural logs of the Bayes factors for those additional retrievals are presented in Table 4. It can be seen that the data of HST/WFC3/G141 (1.1–1.6 μm) requires the disequilibrium chemistry condition most for the case of HD 209458b while it is also important for the HST/STIS data (0.3–0.9 μm). We have confirmed that the best-fit parameter set, which yields the minimum χ^2 when compared to the observed data, from the equilibrium retrieval explains the observed 1.3–1.6 μm feature by H_2O alone. On the other hand, in the disequilibrium retrieval case, NH_3 also partially contributes to reproducing the feature, yielding a better match to the observed data and thus demonstrating the preferability of the disequilibrium retrieval. Here we mention that this slight evidence regarding the NH_3 feature was already noted by MacDonald & Madhusudhan (2017), who used the same data analyzed by Sing et al. (2016) for their retrieval simulations and raised the possibility of disequilibrium chemistry playing a role in the atmosphere of this planet.

Recently, Giacobbe et al. (2021) performed high-resolution transmission spectroscopy of HD 209458b and reported the de-

tection of six species, H_2O , CO , HCN , CH_4 , NH_3 , and C_2H_2 . In their analysis, the disequilibrium scenario was strongly disfavored, though they did not deny the possibility that disequilibrium processes were in effect to some extent. This discrepancy may partly be because they assumed specific thermal and abundance profiles for their disequilibrium scenario while we allow those profiles to vary within our retrieval.

Next, regarding WASP-39b, noticeable differences are found around 0.3–0.5, 2.7, 4.3, and 15 μm (see Fig. 1b). In the case of the equilibrium retrieval (orange line), the favored cloud distributions contribute to flattening the Rayleigh scattering slope and fail to reproduce the observed steepness of the optical slope. The small difference at 2.7 μm arises from the smaller H_2O abundance in the disequilibrium retrieval case (compare the purple thick solid line and purple thick dashed line in Fig. 2b). Due to the absence of CO_2 in the upper atmosphere (gray thick solid line in the same figure), its strong features at 4.3 and 15 μm hardly exist in the disequilibrium retrieval case (blue line in Fig. 1b).

For the retrieved thermal profiles, although the number of samples is limited, a higher temperature in the lower atmosphere

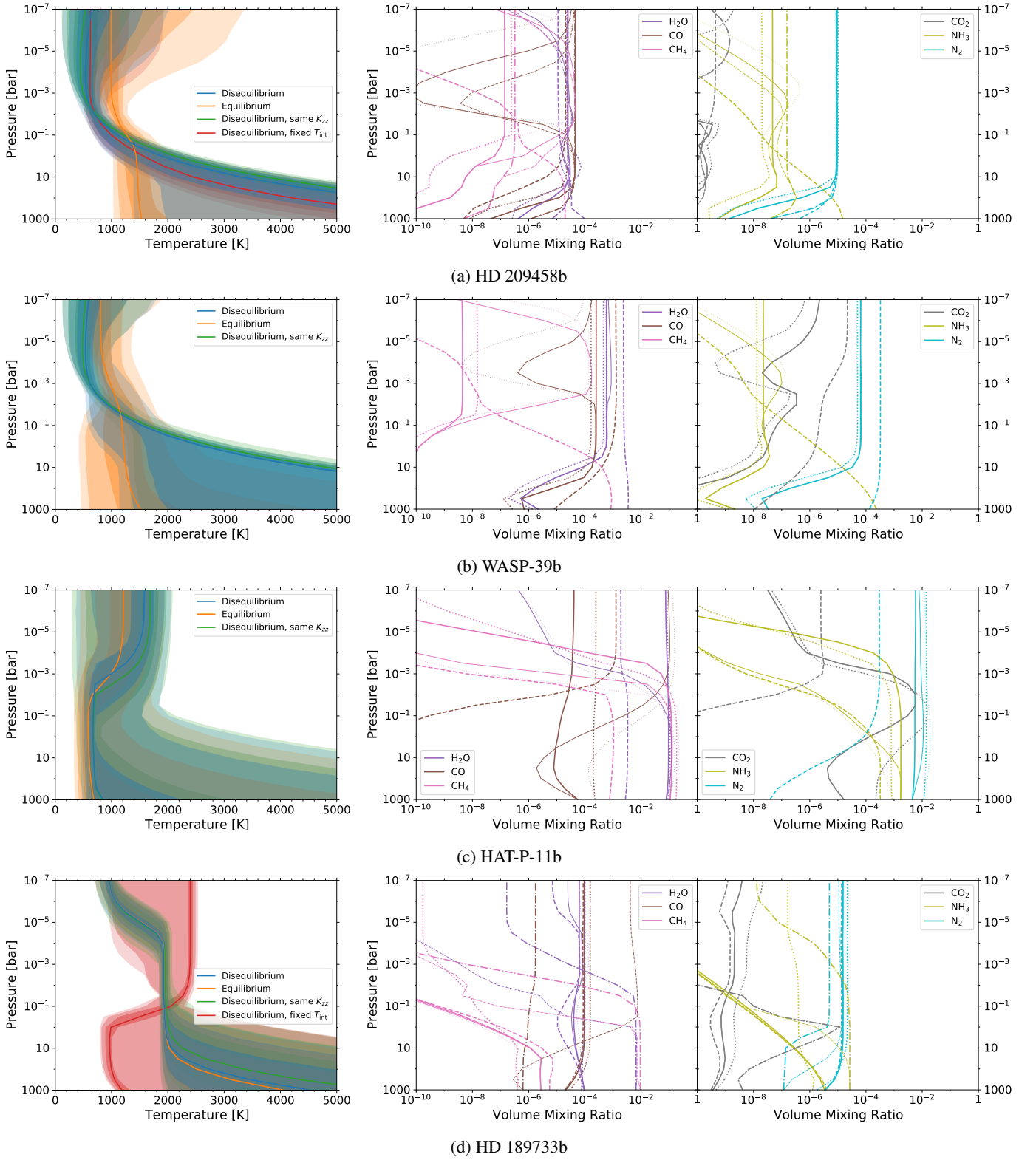


Fig. 2: Atmospheric profiles for four representative planets, while those for the other planets are presented in Fig. A.1 of Appendix A. (Left) Pressure–temperature profiles retrieved from the standard disequilibrium retrieval (blue), equilibrium retrieval (orange), and disequilibrium retrievals with the same K_{zz} (green) and with fixed T_{int} (red; only shown for planets with masses larger than half Jupiter mass). The solid lines show the median models while the shaded regions indicate the 1, 2, and 3 σ confidence intervals. (Right) Median abundance profiles of H₂O, CO, and CH₄ (left) and those of CO₂, NH₃, and N₂ (right) from the standard disequilibrium retrieval (thick solid lines), equilibrium retrieval (thick dashed lines), and disequilibrium retrievals with the same K_{zz} (thick dotted lines) and with fixed T_{int} (thick dash-dotted lines; only shown for planets with masses larger than half Jupiter mass). For reference, the median abundance profiles for the case where the equilibrium chemistry is imposed are shown with the corresponding thin lines.

Table 3: Natural logs of the Bayes factors between the different retrievals

Planet	$\ln E_{\text{diseq}}/E_{\text{eq}}$	$\ln E_{\text{diseq,same}K_{\text{zz}}}/E_{\text{diseq}}$	$\ln E_{\text{diseq},T_{\text{int}}}/E_{\text{diseq}}$
GJ 436b	1.5	1.8	
GJ 1214b	-1.5	0.15	
GJ 3470b	-3.0	-2.2	
HAT-P-1b	-0.26	-0.62	-0.16
HAT-P-11b	-0.80	-0.57	
HAT-P-12b	-0.12	-2.1	
HAT-P-26b	-1.1	-1.7	
HD 97658b	-1.3	0.28	
HD 189733b	0.025	-0.89	-28
HD 209458b	6.9	-1.0	0.29
WASP-6b	0.073	-1.3	
WASP-12b	0.79	-0.94	-0.37
WASP-17b	-0.32	1.2	
WASP-19b	-0.014	0.38	-0.47
WASP-31b	-0.16	-0.51	
WASP-39b	2.4	0.47	

E_{diseq} , E_{eq} , $E_{\text{diseq,same}K_{\text{zz}}}$, and $E_{\text{diseq},T_{\text{int}}}$ are the Bayesian evidences of the standard disequilibrium retrieval, equilibrium retrieval, and disequilibrium retrievals with the same K_{zz} and with fixed T_{int} , respectively.

Table 4: Natural logs of the Bayes factors between the disequilibrium and equilibrium retrievals for the results without a specific data set for HD 209458b

Data	$\ln E_{\text{diseq}}/E_{\text{eq}}$
all	6.9
without HST/STIS (0.3–0.9 μm)	0.35
without HST/WFC3/G141 (1.1–1.6 μm)	-0.12
without <i>Spitzer</i> /IRAC/Ch1 (3.6 μm)	6.8
without <i>Spitzer</i> /IRAC/Ch2 (4.5 μm)	6.9

is favored for the disequilibrium retrieval, while the equilibrium retrieval prefers an isothermal-like profile for several planet samples such as HD 209458b, WASP-39b, GJ 1214b, GJ 3470b, HAT-P-26b, and HD 97658b (see Figs. 2 and A.1). We speculate that this is due to the absence of NH_3 and/or CH_4 absorption features for some of the above planets. This is because if moderate vertical diffusion is imposed for the cool lower atmosphere, such as the equilibrium retrieval cases of the above planets, their abundances would be quenched to the larger values because of their stability at low temperatures and high pressures. Thus, the temperature in the lower atmosphere needs to be increased to reduce their abundances.

The planets for which at least one of the retrieved parameters differs by more than 1σ between the standard disequilibrium and equilibrium retrievals are GJ 436b, GJ 1214b, GJ 3470b, HAT-P-11b, HAT-P-12b, HAT-P-26b, HD 209458b, WASP-6b, and WASP-39b, and their differences are summarized in Table 5. Aside from HD 209458b and WASP-39b, some differences are also found for HAT-P-11b and GJ 436b. For HAT-P-11b, the median values of C/O ratio and metallicity differ by 2.9 and 1.4σ , respectively. While the retrieved C/O ratio from the disequilibrium retrieval is $0.82^{+0.26}_{-0.42}$, that from the equilibrium retrieval is $0.27^{+0.19}_{-0.12}$. For the metallicity, the retrieved values from the disequilibrium and equilibrium retrievals are $\log_{10}(Z [\text{dex}]) = 2.39^{+0.27}_{-0.34}$ and $0.67^{+1.24}_{-0.68}$, respectively. For this planet, even though the retrieved eddy diffusion coefficient is relatively small ($\log_{10}(K_{\text{zz}}^{\text{Ch}} [\text{cm}^2 \text{s}^{-1}]) = 3.74^{+2.67}_{-2.29}$), because of

the somewhat low temperature, disequilibrium chemistry plays an important role (compare the thick and thin solid lines in Fig. 2c). However, the quite small value of the natural log of the Bayes factor in Table 3 indicates that the retrieved parameters from the disequilibrium retrieval are never favored over those from the equilibrium case and vice versa. A further observational constraint is needed to determine the atmospheric properties of this planet. For this purpose, the search for the CO_2 feature at $4.3 \mu\text{m}$ is promising because of its absence in the disequilibrium retrieval case (Fig. 1c). For GJ 436b, while the irradiation parameter from the equilibrium retrieval is $0.01^{+0.01}_{-0.01}$, that from the disequilibrium retrieval is $0.06^{+0.06}_{-0.04}$, resulting in a 4.5σ difference of this parameter and different retrieved thermal structure (Fig. A.1e). However, as for the case of HAT-P-11b, the natural log of the Bayes factor is too small to draw a firm conclusion on the parameter. High-precision observations in the optical wavelength range, where the spectra from the two retrievals show a difference, would be promising to distinguish this. These examples raise the possibility that ignoring the effect of disequilibrium chemistry can lead to an incorrect constraint on the atmospheric properties.

3.2. Comparison of disequilibrium retrievals with and without imposing the same K_{zz} for chemistry and cloud calculations

In this subsection, we compare the results from the standard disequilibrium retrieval and a retrieval where the condition $K_{\text{zz}}^{\text{Ch}} = K_{\text{zz}}^{\text{Cl}}$ is imposed to examine how this affects the retrieval of parameters. As shown in the third column of Table 3, the absolute values of the natural logs of the Bayes factors between the two retrievals are almost negligible for all of our samples (cf. Trotta 2008), indicating that the retrieved parameters from either of the two retrievals are barely favored over those from the other.

The planets for which at least one of the retrieved parameters differs by more than 1σ between the same- K_{zz} and standard disequilibrium retrievals, and their differences are summarized in Table 6. As expected, employing the condition $K_{\text{zz}}^{\text{Ch}} = K_{\text{zz}}^{\text{Cl}}$ strongly affects the retrieval of these two parameters and the cloud nu-

Table 5: Retrieved parameters with more than 1σ difference between the standard disequilibrium (diseq.) and equilibrium (eq.) retrievals

Planet	Parameter	Value from diseq.	Value from eq.	Difference
GJ 436b	f_{irr}	$0.06^{+0.06}_{-0.04}$	$0.01^{+0.01}_{-0.01}$	4.5σ
	$\log_{10}(\kappa_{\text{IR}} [\text{cm}^2 \text{g}^{-1}])$	$-1.51^{+1.79}_{-1.63}$	$0.28^{+2.39}_{-1.78}$	1.0σ
	Z [dex]	$1.63^{+0.26}_{-0.34}$	$1.25^{+0.32}_{-0.36}$	1.2σ
GJ 1214b	$\log_{10}(T_{\text{int}} [K])$	$2.15^{+0.36}_{-0.43}$	$1.54^{+0.48}_{-0.36}$	1.3σ
	$R_{\text{ref}} [R_J]$	$0.24^{+0.00}_{-0.00}$	$0.25^{+0.00}_{-0.00}$	1.3σ
GJ 3470b	$\log_{10}(\kappa_{\text{IR}} [\text{cm}^2 \text{g}^{-1}])$	$-1.45^{+1.67}_{-1.01}$	$-2.34^{+0.83}_{-0.85}$	1.1σ
	$\log_{10}(T_{\text{int}} [K])$	$2.53^{+0.47}_{-0.76}$	$1.72^{+0.51}_{-0.46}$	1.6σ
	$R_{\text{ref}} [R_J]$	$0.32^{+0.01}_{-0.01}$	$0.33^{+0.01}_{-0.01}$	2.0σ
HAT-P-11b	C/O	$0.82^{+0.26}_{-0.42}$	$0.27^{+0.19}_{-0.12}$	2.9σ
	Z [dex]	$2.39^{+0.27}_{-0.34}$	$0.67^{+1.24}_{-0.68}$	1.4σ
	$R_{\text{ref}} [R_J]$	$0.39^{+0.00}_{-0.00}$	$0.39^{+0.00}_{-0.00}$	1.2σ
HAT-P-12b	Z [dex]	$-0.19^{+1.64}_{-0.61}$	$1.55^{+0.28}_{-1.52}$	1.1σ
HAT-P-26b	$R_{\text{ref}} [R_J]$	$0.46^{+0.02}_{-0.02}$	$0.49^{+0.01}_{-0.01}$	1.5σ
HD 209458b	$\log_{10} \gamma$	$0.77^{+0.80}_{-1.15}$	$-0.77^{+0.45}_{-0.37}$	3.4σ
	f_{irr}	$0.01^{+0.01}_{-0.00}$	$0.09^{+0.05}_{-0.04}$	2.3σ
	$\log_{10}(\kappa_{\text{IR}} [\text{cm}^2 \text{g}^{-1}])$	$1.51^{+1.59}_{-1.91}$	$-1.49^{+0.80}_{-0.77}$	3.7σ
	$\log_{10}(T_{\text{int}} [K])$	$2.11^{+0.42}_{-0.39}$	$1.59^{+0.46}_{-0.39}$	1.1σ
	C/O	$0.50^{+0.21}_{-0.28}$	$0.19^{+0.14}_{-0.07}$	2.3σ
	$R_{\text{ref}} [R_J]$	$1.35^{+0.02}_{-0.01}$	$1.36^{+0.01}_{-0.01}$	2.1σ
	$\log_{10}(K_{\text{zz}}^{\text{Cl}} [\text{cm}^2 \text{s}^{-1}])$	$5.46^{+0.26}_{-0.30}$	$5.89^{+0.13}_{-0.15}$	2.9σ
WASP-6b	$\log_{10}(T_{\text{int}} [K])$	$1.91^{+0.41}_{-0.58}$	$1.49^{+0.34}_{-0.30}$	1.3σ
	$\log_{10}(K_{\text{zz}}^{\text{Cl}} [\text{cm}^2 \text{s}^{-1}])$	$7.27^{+1.12}_{-1.11}$	$8.15^{+1.99}_{-0.82}$	1.1σ
WASP-39b	$\log_{10} \gamma$	$0.50^{+1.03}_{-2.01}$	$-0.90^{+1.30}_{-0.49}$	1.1σ
	f_{irr}	$0.02^{+0.03}_{-0.01}$	$0.07^{+0.07}_{-0.04}$	1.6σ
	$\log_{10}(\kappa_{\text{IR}} [\text{cm}^2 \text{g}^{-1}])$	$1.44^{+1.66}_{-2.06}$	$-0.38^{+0.98}_{-2.37}$	1.9σ
	$\log_{10}(T_{\text{int}} [K])$	$2.04^{+0.43}_{-0.34}$	$1.52^{+0.48}_{-0.35}$	1.1σ
	Si/O	$0.01^{+0.01}_{-0.01}$	$0.06^{+0.06}_{-0.04}$	1.2σ
	Z [dex]	$-0.04^{+0.35}_{-0.26}$	$0.73^{+0.75}_{-0.65}$	1.2σ
	$R_{\text{ref}} [R_J]$	$1.20^{+0.05}_{-0.02}$	$1.27^{+0.03}_{-0.03}$	2.5σ
	$\log_{10}(g [\text{cm s}^{-2}])$	$2.78^{+0.03}_{-0.05}$	$2.73^{+0.04}_{-0.06}$	1.1σ
	$\log_{10}(K_{\text{zz}}^{\text{Cl}} [\text{cm}^2 \text{s}^{-1}])$	$5.59^{+0.48}_{-0.38}$	$6.44^{+0.31}_{-0.47}$	1.8σ

cleation rate. Large ($\geq 3\sigma$) differences are found for GJ 436b, GJ 1214b, HAT-P-12b, HD 189733b, HD 209458b, WASP-17b, WASP-19b, and WASP-39b. For all the planets, those differences are for $K_{\text{zz}}^{\text{Cl}}$ and $K_{\text{zz}}^{\text{Ch}}$ as well as $\dot{\Sigma}$ for HD 189733b.

For HD 209458b, for which we find an indication of disequilibrium chemistry from the comparison between the standard disequilibrium and equilibrium retrievals in § 3.1, the retrieved value of $\log_{10}(K_{\text{zz}}^{\text{Ch}} [\text{cm}^2 \text{s}^{-1}])$ decreases from $13.12^{+1.39}_{-4.61}$ to $4.17^{+1.15}_{-1.05}$ with a 1.9σ difference. Despite this decrease, the spectrum from the same- K_{zz} retrieval (green line in Fig. 1a) still exhibits certain disequilibrium features, as discussed in § 3.1, such as those at 2.5–4.0, 6.5–9, and 9–13 μm .

Also, for WASP-39b, for which we also find an indication of disequilibrium chemistry in § 3.1, the retrieved spectra, thermal structures, abundance profiles, and parameters (see Figs. 1b, 2b, and B.1b) are quite similar to the standard disequilibrium re-

trieval case. Thus, our findings of indications of disequilibrium chemistry for HD 209458b and WAS-39b still hold.

3.3. Comparison of disequilibrium retrievals with and without a fixed intrinsic temperature

In this subsection, we compare the results from the standard disequilibrium retrieval and that with a fixed intrinsic temperature. The motivation to fix the intrinsic temperature is based on the expectation that the retrieval of the chemical eddy diffusion coefficient might degenerate with the intrinsic temperature since the quenching often happens in the deeper atmosphere where the intrinsic temperature has a large influence on the thermal structure. Despite our expectation, however, such a correlation is not found (see Fig. B.1), which may be due to the limits of the current observational precision. The correlation co-

Table 6: Retrieved parameters with more than 1σ difference between the same- K_{zz} and standard disequilibrium retrievals

Planet	Parameter	Value from same- K_{zz}	Value from standard	Difference
GJ 436b	$\log_{10}(K_{zz}^{\text{Cl}} [\text{cm}^2 \text{s}^{-1}])$	$2.37^{+1.73}_{-1.54}$	$5.33^{+0.40}_{-0.23}$	12.9σ
	$\log_{10}(K_{zz}^{\text{Ch}} [\text{cm}^2 \text{s}^{-1}])$	$2.37^{+1.73}_{-1.54}$	$7.77^{+4.77}_{-5.05}$	1.1σ
GJ 1214b	$\log_{10}(K_{zz}^{\text{Cl}} [\text{cm}^2 \text{s}^{-1}])$	$14.07^{+0.62}_{-6.55}$	$6.72^{+2.06}_{-0.88}$	3.6σ
	$\log_{10}(K_{zz}^{\text{Ch}} [\text{cm}^2 \text{s}^{-1}])$	$14.07^{+0.62}_{-6.55}$	$8.83^{+3.98}_{-5.05}$	1.3σ
HAT-P-11b	$\log_{10}(K_{zz}^{\text{Cl}} [\text{cm}^2 \text{s}^{-1}])$	$5.61^{+0.96}_{-2.58}$	$6.28^{+0.77}_{-0.64}$	1.0σ
HAT-P-12b	$\log_{10}(\kappa_{\text{IR}} [\text{cm}^2 \text{g}^{-1}])$	$-2.27^{+0.85}_{-0.89}$	$-3.09^{+0.72}_{-0.61}$	1.2σ
	$\log_{10}(T_{\text{int}} [K])$	$2.86^{+0.20}_{-0.26}$	$1.97^{+0.66}_{-0.59}$	1.4σ
	Si/O	$0.03^{+0.04}_{-0.02}$	$0.14^{+0.09}_{-0.09}$	1.2σ
	Z [dex]	$1.85^{+0.23}_{-0.26}$	$-0.19^{+1.64}_{-0.61}$	1.2σ
	$R_{\text{ref}} [R_J]$	$0.84^{+0.02}_{-0.02}$	$0.86^{+0.01}_{-0.02}$	1.1σ
	$\log_{10}(K_{zz}^{\text{Cl}} [\text{cm}^2 \text{s}^{-1}])$	$13.87^{+0.84}_{-2.48}$	$10.18^{+1.14}_{-1.45}$	3.2σ
	$\log_{10}(K_{zz}^{\text{Ch}} [\text{cm}^2 \text{s}^{-1}])$	$13.87^{+0.84}_{-2.48}$	$2.66^{+1.80}_{-1.67}$	6.2σ
HD 97658b	$\log_{10}(K_{zz}^{\text{Cl}} [\text{cm}^2 \text{s}^{-1}])$	$12.53^{+1.40}_{-1.83}$	$10.53^{+0.91}_{-1.18}$	2.2σ
	$\log_{10}(K_{zz}^{\text{Ch}} [\text{cm}^2 \text{s}^{-1}])$	$12.53^{+1.40}_{-1.83}$	$6.92^{+4.93}_{-4.61}$	1.1σ
HD 189733b	$\log_{10}(K_{zz}^{\text{Cl}} [\text{cm}^2 \text{s}^{-1}])$	$13.04^{+0.72}_{-0.91}$	$11.21^{+0.51}_{-1.21}$	3.6σ
	$\log_{10}(\Sigma [\text{cm}^2 \text{s}^{-1}])$	$-10.98^{+2.78}_{-1.69}$	$-13.99^{+0.84}_{-1.38}$	3.6σ
	$\log_{10}(K_{zz}^{\text{Ch}} [\text{cm}^2 \text{s}^{-1}])$	$13.04^{+0.72}_{-0.91}$	$5.43^{+5.90}_{-3.44}$	1.3σ
HD 209458b	C/O	$0.19^{+0.12}_{-0.06}$	$0.50^{+0.21}_{-0.28}$	1.1σ
	$\log_{10}(K_{zz}^{\text{Cl}} [\text{cm}^2 \text{s}^{-1}])$	$4.17^{+1.15}_{-1.05}$	$5.46^{+0.26}_{-0.30}$	4.3σ
	$\log_{10}(K_{zz}^{\text{Ch}} [\text{cm}^2 \text{s}^{-1}])$	$4.17^{+1.15}_{-1.05}$	$13.12^{+1.39}_{-4.61}$	1.9σ
WASP-12b	$\log_{10}(K_{zz}^{\text{Cl}} [\text{cm}^2 \text{s}^{-1}])$	$11.35^{+2.16}_{-2.08}$	$9.94^{+1.28}_{-1.34}$	1.1σ
WASP-17b	$\log_{10}(K_{zz}^{\text{Cl}} [\text{cm}^2 \text{s}^{-1}])$	$2.82^{+2.13}_{-1.88}$	$5.70^{+0.55}_{-0.46}$	6.2σ
WASP-19b	$\log_{10}(K_{zz}^{\text{Cl}} [\text{cm}^2 \text{s}^{-1}])$	$3.32^{+2.29}_{-2.11}$	$6.20^{+1.66}_{-0.78}$	3.7σ
WASP-39b	$\log_{10}(K_{zz}^{\text{Cl}} [\text{cm}^2 \text{s}^{-1}])$	$4.27^{+1.23}_{-1.01}$	$5.59^{+0.48}_{-0.38}$	3.5σ
	$\log_{10}(K_{zz}^{\text{Ch}} [\text{cm}^2 \text{s}^{-1}])$	$4.27^{+1.23}_{-1.01}$	$8.61^{+3.68}_{-4.22}$	1.0σ

Note that K_{zz} derived from the same- K_{zz} retrieval, which is used in both cloud and chemistry calculations, is compared to K_{zz}^{Cl} and K_{zz}^{Ch} from the standard disequilibrium retrieval.

efficients between $\log_{10}(T_{\text{int}} [K])$ and $\log_{10}(K_{zz}^{\text{Cl}} [\text{cm}^2 \text{s}^{-1}])$ are 0.12, 0.071, 0.17, 0.0037, and 0.10 for HAT-P-1b, HD 189733b, HD 209458b, WASP-12b, and WASP-19b, respectively. We note that for all the five targets to which we applied T_{int} -fixed retrieval, the standard retrieval favors a lower value of T_{int} than that inferred from the formula derived by Thorngren et al. (2019) (see Table 7). As shown in the fourth column of Table 3, the absolute values of the natural logs of the Bayes factors between the two retrievals are quite small (cf. Trotta 2008) except for HD 189733b.

HD 189733b exhibits significantly smaller Bayesian evidence of disequilibrium retrieval with fixed T_{int} , indicating that the retrieved parameters from that retrieval are strongly ($\geq 7.8\sigma$) disfavored compared to those from the standard disequilibrium retrieval. The significant difference in the Bayesian evidence is partly due to the worse fit to the observed data points in the bluest part (0.3–0.5 μm) for the T_{int} -fixed retrieval (red line in Fig. 1d). This discrepancy is due to the different retrieved parameters for the clouds. We note, however, that there is room for discussion regarding the quite steep optical slope of this planet (Pont et al. 2013). Several origins aside from the planetary atmosphere, such as an unknown systematic instrument offset between the optical

and near-infrared or the presence of starspots on the host star (e.g., Oshagh et al. 2014, 2020) have been proposed as being capable of artificially producing such a steep slope in the planetary spectrum.

Comparing the retrieved spectra of HD 189733b from the two retrievals, differences can also be found above 8.0 μm . In the standard disequilibrium retrieval case (blue line), cloud features exist around 9.4 and 20 μm while the C_2H_2 absorption feature is visible at 13.6 μm in the T_{int} -fixed retrieval case (red line). A striking difference is also found in the retrieved thermal structure (see Fig. 2d). A strong thermal inversion is retrieved from the T_{int} -fixed retrieval (red line), whereas no such inversion is derived from the standard disequilibrium retrieval (blue line). We note that in our retrieval, we retrieved the parameters regarding the thermal structure independently from the atmospheric constituents. A retrieval employing a thermal structure consistent with the opacity of the atmospheric composition will be the subject of future work.

The retrieved parameters with more than 1σ difference between the T_{int} -fixed and standard disequilibrium retrievals are summarized in Table 7. Indeed, quite significant differences are found for the parameters of HD 189733b.

Table 7: Retrieved parameters with more than 1σ difference between the T_{int} -fixed and standard disequilibrium retrievals

Planet	Parameter	Value from T_{int} -fixed	Value from standard	Difference
HAT-P-1b	$\log_{10}(T_{\text{int}} [K])$	2.68	$1.81^{+0.66}_{-0.51}$	1.3σ
HD 189733b	$\log_{10} \gamma$	$1.66^{+0.15}_{-0.08}$	$-1.31^{+0.10}_{-0.16}$	30.1σ
	$\log_{10}(\kappa_{\text{IR}} [\text{cm}^2 \text{g}^{-1}])$	$-3.81^{+0.28}_{-0.14}$	$3.05^{+0.38}_{-0.35}$	19.8σ
	$\log_{10}(T_{\text{int}} [K])$	2.58	$1.51^{+0.30}_{-0.30}$	3.6σ
	C/O	$1.21^{+0.06}_{-0.09}$	$0.47^{+0.24}_{-0.22}$	3.1σ
	Si/O	$0.03^{+0.02}_{-0.01}$	$0.12^{+0.07}_{-0.06}$	1.5σ
	Z [dex]	$1.06^{+0.18}_{-0.23}$	$-0.56^{+0.46}_{-0.26}$	3.5σ
	$\log_{10}(g [\text{cm s}^{-2}])$	$3.30^{+0.02}_{-0.02}$	$3.38^{+0.02}_{-0.02}$	4.5σ
	$\log_{10}(K_{zz}^{\text{Cl}} [\text{cm}^2 \text{s}^{-1}])$	$7.08^{+0.17}_{-0.13}$	$11.21^{+0.51}_{-1.21}$	3.4σ
	$\log_{10}(\Sigma [\text{cm}^2 \text{s}^{-1}])$	$-7.06^{+0.05}_{-0.11}$	$-13.99^{+0.84}_{-1.38}$	8.2σ
HD 209458b	$\log_{10}(K_{zz}^{\text{Ch}} [\text{cm}^2 \text{s}^{-1}])$	$12.62^{+1.16}_{-0.68}$	$5.43^{+5.90}_{-3.44}$	1.2σ
	$\log_{10} \gamma$	$-1.03^{+1.62}_{-0.71}$	$0.77^{+0.80}_{-1.15}$	1.6σ
	$\log_{10}(\kappa_{\text{IR}} [\text{cm}^2 \text{g}^{-1}])$	$-1.35^{+0.64}_{-0.44}$	$1.51^{+1.59}_{-1.91}$	1.5σ
	$\log_{10}(T_{\text{int}} [K])$	2.75	$2.11^{+0.42}_{-0.39}$	1.5σ
WASP-12b	$\log_{10}(T_{\text{int}} [K])$	2.71	$2.03^{+0.58}_{-0.62}$	1.2σ
WASP-19b	$\log_{10}(T_{\text{int}} [K])$	2.81	$1.81^{+0.70}_{-0.51}$	1.4σ

3.4. Trend of the retrieved parameters

In this subsection, we explore the trend of the atmospheric parameters derived from our retrieval calculations.

3.4.1. Eddy diffusion coefficient

Figure 3 shows the retrieved values of the eddy diffusion coefficients as a function of the equilibrium temperature for our samples (top panel for the chemical eddy diffusion coefficient K_{zz}^{Ch} and bottom panel for the cloud eddy diffusion coefficient K_{zz}^{Cl}). First, neither K_{zz}^{Ch} (blue circle points in the top panel) nor K_{zz}^{Cl} (purple triangle points in the bottom panel) from the standard disequilibrium retrieval exhibits any clear trend over the equilibrium temperature, at least for the current observed data. On the other hand, a larger diffusion coefficient for higher temperature has been predicted from both theory and numerical GCM simulations because of the increasing speed of vertical winds (Komacek et al. 2019). This trend is also tentatively indicated by the recent analysis of the *Spitzer* transit depths of about fifty gas giants by Baxter et al. (2021). The higher observational precision achievable with the *James Webb* Space Telescope (JWST; Gardner et al. 2006) and the Atmospheric Remote-sensing Infrared Exoplanet Large-survey (Ariel; Tinetti et al. 2018) will enable us to further explore such predictions.

Compared to K_{zz}^{Ch} (blue circle points), K_{zz}^{Cl} (purple triangle points) is retrieved with much smaller uncertainties due to the strong effect of the diffusion coefficient on the cloud structure (Gao & Benneke 2018; Ormel & Min 2019). Also, the comparison of K_{zz}^{Cl} between the standard disequilibrium and equilibrium retrievals (purple and orange triangle points in the bottom panel) shows that they are quite similar.

Next, K_{zz} from the disequilibrium retrieval employing the condition $K_{zz}^{\text{Ch}} = K_{zz}^{\text{Cl}}$ (green square points in both panels) does not exhibit any clear trend over the equilibrium temperature either. In some cases, the 1σ uncertainty range of K_{zz} from the same- K_{zz} retrieval lies outside the median values of K_{zz}^{Ch} and K_{zz}^{Cl}

from the standard disequilibrium retrieval. This is probably because we have imposed the strong condition $K_{zz}^{\text{Ch}} = K_{zz}^{\text{Cl}}$ with a constant value throughout the atmosphere even though the location of the quenching and clouds affecting the spectrum are usually different and several orders of magnitude difference of K_{zz} within the atmosphere is expected from GCM simulations (Zhang & Showman 2018; Komacek et al. 2019).

Among our samples, HD 209458b has a markedly large retrieved K_{zz}^{Ch} (blue circle point) from the standard disequilibrium retrieval. When the condition $K_{zz}^{\text{Ch}} = K_{zz}^{\text{Cl}}$ is imposed, the retrieved value of K_{zz} (green square point) decreases, especially when compared to K_{zz}^{Ch} . However, as we mentioned in § 3.2, even with this small K_{zz} , the retrieved spectrum still exhibits disequilibrium features. Thus, we propose that this planet is an ideal target for studying disequilibrium chemistry in exoplanet atmospheres.

K_{zz}^{Ch} retrieved from the T_{int} -fixed disequilibrium retrieval (red circle points in the top panel) is tightly constrained compared to the standard disequilibrium retrieval for HD 189733b and HD 209458b, while this is not the case for HAT-P-1b, WASP-12b, and WASP-19b. There are several possible reasons for this. First, for HD 189733b, the value of T_{int} we have fixed with the formula of Thorngren et al. (2019) is different from the retrieved value from the standard equilibrium retrieval by more than 3σ (see Table 7), and the T_{int} -fixed disequilibrium retrieval results in a different thermal profile with high temperatures in the upper atmosphere (see Fig. 2d). This requires a larger K_{zz}^{Ch} to reproduce the observed amplitude of the $1.4 \mu\text{m}$ H₂O absorption feature by overcoming its thermal dissociation due to high temperatures (compare the purple thick dash-dotted line and purple thin dash-dotted line in Fig. 2d). On the other hand, in the case of the standard disequilibrium retrieval, the retrieved small value of K_{zz}^{Ch} indicates that disequilibrium chemistry is not significantly preferred over equilibrium chemistry. This is also seen in the almost consistent median abundance profiles between the standard disequilibrium and equilibrium retrievals (compare the thick solid lines and dashed lines in the right panel of Fig. 2d).

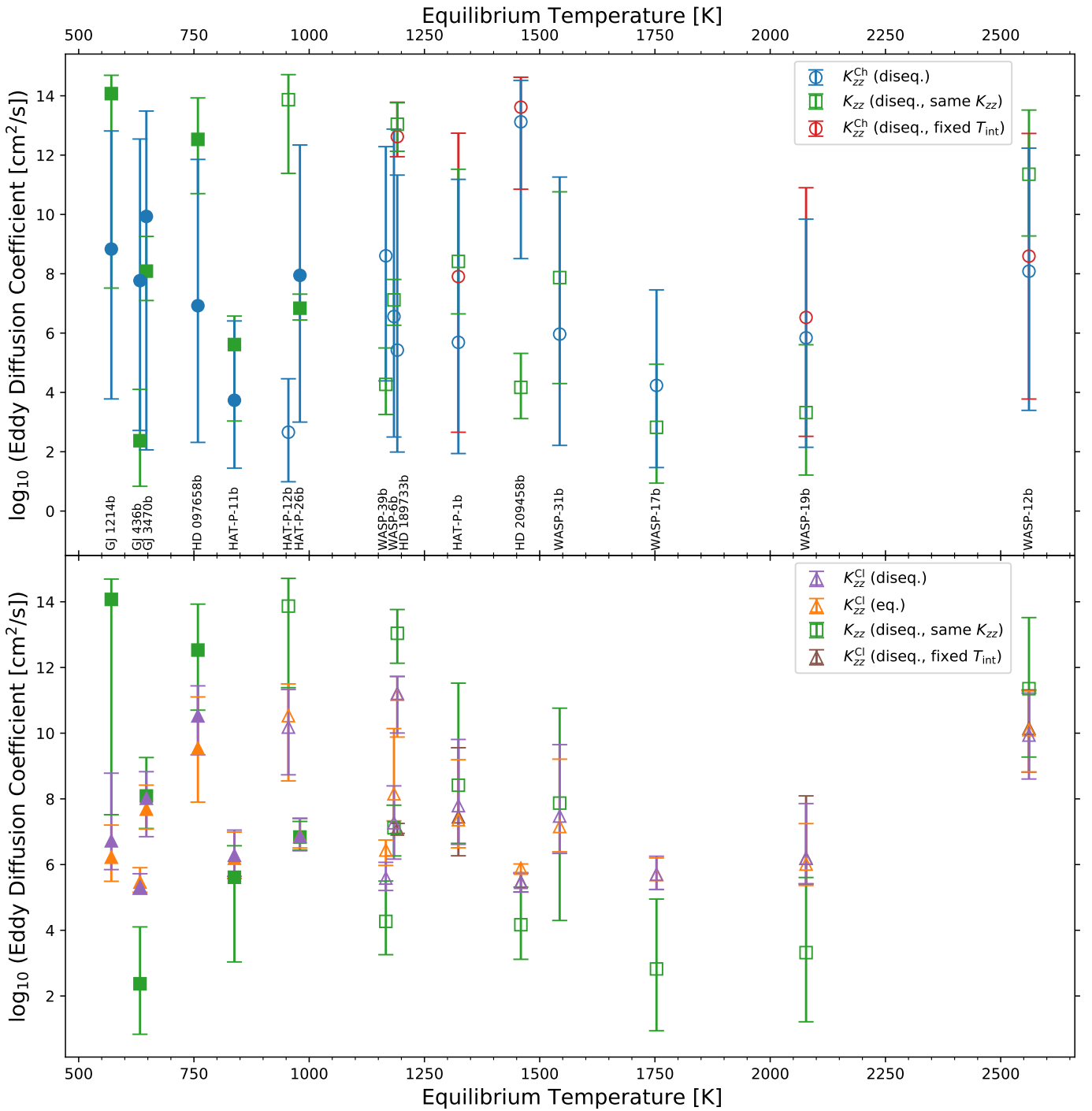


Fig. 3: (Top) Eddy diffusion coefficients for the chemical structure simulations, K_{zz}^{Ch} , retrieved from the standard disequilibrium retrieval (blue circle points) and that with fixed T_{int} (red circle points; only shown for the planets with masses larger than half Jupiter mass). Also shown are the eddy diffusion coefficients used for both chemistry and cloud simulations in the same- K_{zz} retrieval (green square points). (Bottom) Eddy diffusion coefficients for the cloud structure simulations, K_{zz}^{Cl} , retrieved from the standard disequilibrium retrieval (purple triangle points), equilibrium retrieval (orange triangle points), and disequilibrium retrieval with fixed T_{int} (brown triangle points; again, only shown for the planets with masses larger than half Jupiter mass). The eddy diffusion coefficients used for both chemistry and cloud simulations in the same- K_{zz} retrieval are also plotted (green square points, as in the top panel). The unfilled points indicate our hot Jupiter samples, while the filled points are the Neptune samples, which we define as masses smaller than 0.1 times the Jupiter mass. The error bars indicate 1 σ uncertainty from the retrievals.

Thus, K_{zz}^{Ch} remains unconstrained while it needs to be small enough. Next, for HD 209458b, disequilibrium chemistry plays an important role in its atmosphere, unlike the cases of WASP-

12b and WASP-19b (see Figs. 2 and A.1). Since the quenching happens in the deep atmosphere where the intrinsic temperature has a big influence on the thermal structure, the value of K_{zz}^{Ch}

could be tightly constrained when T_{int} is fixed to a certain value for the atmospheres with disequilibrium chemistry. Given the somewhat stronger constraint on K_{zz}^{Ch} for HD 209458b, we ideally expect a correlation between T_{int} and K_{zz}^{Ch} in the results of the standard disequilibrium retrieval for this planet, which we do not find, as mentioned in § 3.3. We consider that the complexity of the retrieval we have performed, namely retrieval with more than ten retrieval parameters, could cause this apparent absence of the correlation. Moreover, we speculate that the precision of the observational data is also related because if the observational uncertainty is large, it would not have an impact on the constraint on the parameters even if we fix any of the parameters. The observational data for HD 189733b and HD 209458b are relatively precise when compared to those of the other three planets. Indeed, we have found that when all the observational errors are artificially reduced to half their values, K_{zz}^{Ch} becomes somewhat tightly constrained for HAT-P-1b while not for WASP-12b and WASP-19b when T_{int} is fixed. In the atmosphere of HAT-P-1b, disequilibrium chemistry has a modest impact (see Fig. A.1h). Future investigations are needed to draw firm conclusions about the points raised.

Finally, K_{zz}^{Cl} retrieved from the T_{int} -fixed disequilibrium retrieval (brown triangle points in the bottom panel) are largely similar to those of the standard disequilibrium retrieval except for HD 189733b, for which the retrieved thermal structure differs significantly (see Fig. 2d).

3.4.2. Metallicity and C/O ratio

Figure 4 shows the derived values of (a) metallicity and (b) C/O ratio from our four different retrievals as a function of the planet mass. For most planets, the values of the two parameters derived from the different retrievals are consistent within the 1σ error. As for the metallicity trend, our results generally agree with the previous studies that found a tentative trend of higher metallicity with decreasing planet mass, such as seen for the solar system planets (Wakeford et al. 2017; Nikolov et al. 2018; Welbanks et al. 2019). On the other hand, we see no clear trend for the C/O ratio, at least for the current observational precision, which is also consistent with previous work (Min et al. 2020). Since both metallicity and C/O ratio are regarded as important indicators of planet formation (Öberg et al. 2011; Eistrup et al. 2016; Morasini et al. 2016; Eistrup et al. 2018; Notsu et al. 2020), future higher-precision observations are essential to further explore the trends of these parameters toward understanding the origin and formation mechanism of planets.

4. Discussion

4.1. Eddy diffusion coefficient

4.1.1. Range used in retrieval

As we have mentioned in § 2.3, for some of the cooler planets of our samples, the lower bound of the K_{zz}^{Ch} range adopted in the retrievals, namely $10^0 \text{ cm}^2 \text{ s}^{-1}$, is not sufficiently small for all the species to be in chemical equilibrium. To confirm our findings, we have performed additional standard disequilibrium retrievals extending the lower bound of K_{zz}^{Ch} to an extremely small value of $10^{-40} \text{ cm}^2 \text{ s}^{-1}$. We choose this value so that the atmosphere lower than the 0.1 mbar level, which is the lower bound of the

valid pressure range for the chemical timescale formula of Tsai et al. (2018), is in chemical equilibrium when calculated with the best-fit parameter set of the standard disequilibrium retrieval for all of our samples except WASP-39b. We note that while we have found that the best-fit parameter set for WASP-39b requires $K_{zz}^{\text{Ch}} \lesssim 10^{-60} \text{ cm}^2 \text{ s}^{-1}$, the resultant temperature in its upper atmosphere is lower than the lower bound of the valid temperature range for the chemical timescale of Tsai et al. (2018), namely 500 K. Thus it is uncertain whether such a small value of K_{zz}^{Ch} is needed to achieve the equilibrium condition in its atmosphere. Regarding our finding of the indication of disequilibrium chemistry for WASP-39b, we have confirmed that the temperature in the relatively lower atmosphere where the quenching happens is within the validated range, so this does not affect our conclusion.

Figure 5 shows the posterior probability distribution of K_{zz}^{Ch} for (a) HD 209458b, (b) WASP-39b, and (c) HD 189733b. For HD 209458b and WASP-39b, for which we have found indicative evidence of disequilibrium chemistry, the peak of the posterior distribution remains at a similar value regardless of the adopted wider range, ensuring the relatively large values of K_{zz}^{Ch} we have retrieved for these two planets. On the other hand, for all the other planets, as for the case of (c) HD 189733b, we find that adopting a smaller lower bound for the K_{zz}^{Ch} range, the posterior distribution flattens and the median and 1σ confidence interval shift toward smaller values, inferring that the retrieval of K_{zz}^{Ch} is affected by the choice of the K_{zz}^{Ch} range and thus its retrieved value is not reliable. This is consistent with our results that the disequilibrium scenarios are never favored over the equilibrium ones for all of our samples except HD 209458b and WASP-39b in § 3.1.

4.1.2. Profile

While we have used a constant eddy diffusion coefficient throughout the atmosphere in this study, K_{zz} is expected to vary over several orders of magnitude within the atmosphere (Parmentier et al. 2013; Zhang & Showman 2018; Komacek et al. 2019), which is also observed in the atmospheres of the solar system planets (e.g., Allen et al. 1981; Moses et al. 2005). Employing an eddy diffusion coefficient profile, such as an increasing coefficient with decreasing pressure, will be the subject of future work.

4.2. Effect of photochemistry

As mentioned in the introduction, we have ignored photochemistry. Its effect is more significant for cooler atmospheres because of the longer timescale of thermochemical reactions, and the atmospheres of the planets close to the host stars. The UV irradiation from the host star dissociates the molecules such as H_2O in the upper atmosphere. Thus, if we think naively, neglecting the photochemistry effect could lead to an underestimate of the chemical eddy diffusion coefficient needed to reproduce the observed absorption features of molecules such as H_2O .³ On the other hand, in hot ($\gtrsim 1000 \text{ K}$) hydrogen-dominated atmospheres, photodissociation of CO contributes to the formation of additional CO_2 in the upper atmosphere (e.g., Moses et al. 2011; Venot et al. 2012) while in cool ($\lesssim 1000 \text{ K}$) atmospheres,

³ We note that reality is more complex. For example, OH molecules produced by the photodissociation of H_2O react with H_2 , restoring H_2O molecules (Liang et al. 2003). Hydrogen atoms formed by this process can be crucial for atmospheric chemistry.

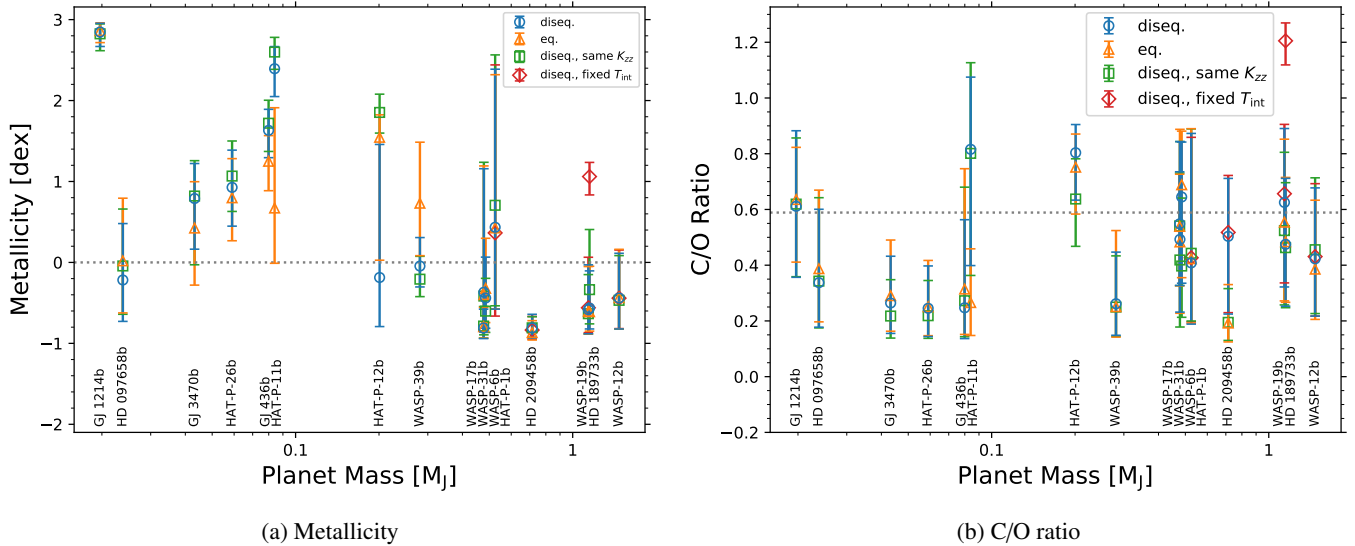


Fig. 4: Atmospheric metallicity (a) and C/O ratio (b) derived from the standard disequilibrium retrieval (blue circle points), equilibrium retrieval (orange triangle points), disequilibrium retrieval with same K_{zz} (green square points), and T_{int} -fixed disequilibrium retrieval (red diamond points; only shown for the planets with masses larger than half Jupiter mass). The solar metallicity and C/O ratio from the solar photospheric elemental abundance ratios of Asplund et al. (2021) are marked with dotted lines for reference.

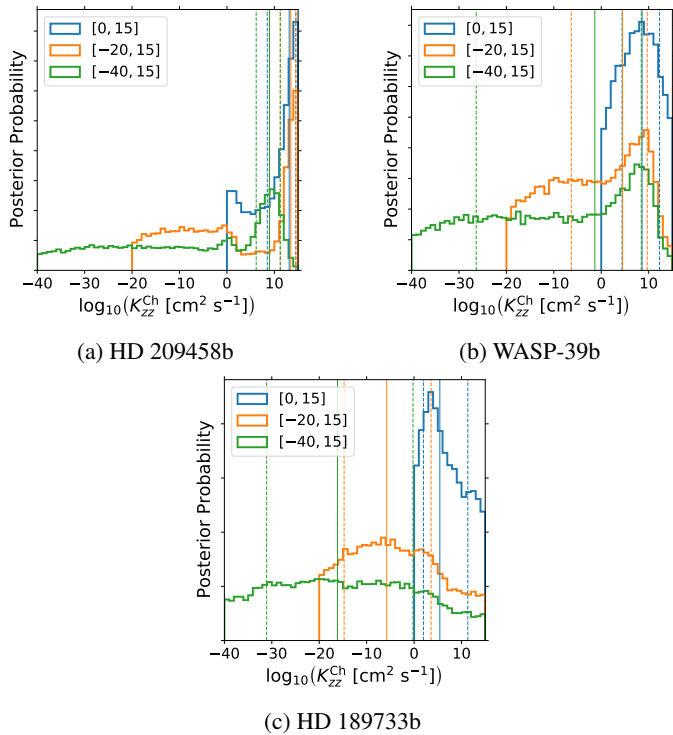


Fig. 5: Posterior probability distribution of $\log_{10}(K_{zz}^{\text{Ch}} [\text{cm}^2 \text{s}^{-1}])$ from the standard disequilibrium retrievals with different ranges adopted, [0, 15] (blue), [-20, 15] (orange), and [-40, 15] (green). The vertical solid and dashed lines indicate the median value and the 1σ confidence interval, respectively.

photodissociation of CH_4 forms both CO_2 and CO at high altitudes (e.g., Miller-Ricci Kempton et al. 2012; Kawashima & Ikoma 2018). Thus, for the spectra with prominent CO_2 and/or CO features, neglecting the photochemistry effect could instead lead to overestimation of the chemical eddy diffusion coefficient.

Among the *Hubble* and *Spitzer* data we have used in this study, CO_2 and CO can exhibit their features in *Spitzer*'s IRAC/Ch2 ($4.5 \mu\text{m}$) band.

To examine the effect of neglecting photochemistry on the observed indications of disequilibrium chemistry, we have performed additional standard disequilibrium and equilibrium retrievals excluding the data of *Spitzer*'s IRAC/Ch2 ($4.5 \mu\text{m}$) band for WASP-39b, while the results of these retrievals for HD 209458b have already been presented in Table 4. We find that disequilibrium chemistry remains favored for both planets HD 209458b and WASP-39b, with natural logs of the Bayes factors of 6.9 and 2.3, respectively. These values are almost the same as those in Table 3, indicating that the features of CO_2 and CO hardly affect the need for disequilibrium chemistry in the atmospheres of those planets. The retrieved values of the chemical eddy diffusion coefficients are $\log_{10}(K_{zz}^{\text{Ch}} [\text{cm}^2 \text{s}^{-1}]) = 13.05^{+1.37}_{-2.45}$ and $8.65^{+3.76}_{-4.34}$ for HD 209458b and WASP-39b, respectively, which are also similar to the retrieved values for the data including IRAC/Ch2 of $13.12^{+1.39}_{-4.61}$ and $8.61^{+3.68}_{-4.22}$. Thus, the retrieved large value of K_{zz}^{Ch} for HD 209458b from the standard disequilibrium retrieval still holds and is not greatly affected by the effect of neglecting photochemistry.

4.3. Additional chemical species

In this study, we have considered the quenching process for the molecules containing the most abundant elements next to hydrogen and helium, namely carbon, oxygen, and nitrogen. Currently, the reaction rate coefficients are less constrained for the molecules consisting of the other elements, while they are also expected to be subject to the quenching effect. Derivation of the chemical timescale for molecules such as H_2S and PH_3 is urgently needed given their relatively good observability and large abundances.

4.4. Effect of photochemical haze

While we have considered the effect of clouds in this study using the model of Ormel & Min (2019), we have ignored the effect of photochemical haze that is also expected to form in the atmospheres of exoplanets (Zahnle et al. 2009; Miller-Ricci Kempton et al. 2012; Hu et al. 2013; Morley et al. 2013, 2015; Zahnle et al. 2016; Gao et al. 2017; Lavvas & Koskinen 2017; Kawashima & Ikoma 2018; Gao et al. 2020). Clouds and haze are expected to have opposite dependences on the eddy diffusivity. A large K_{zz} can raise clouds, which are usually formed in the relatively lower atmosphere, thus resulting in an optically thick atmosphere (Gao & Benneke 2018; Ormel & Min 2019). On the other hand, vigorous mixing efficiently removes photochemical haze from the upper atmosphere making the atmosphere optically thinner (Kawashima & Ikoma 2019; Ohno & Kawashima 2020). Thus, the inclusion of haze particles, which we will leave for future work, might lead to different results, especially for K_{zz} .

4.5. Toward 2D and 3D retrieval modeling with disequilibrium chemistry

In this study, we have considered 1D atmospheres for the sake of simplicity and reducing the computational cost, consistent with most current spectral retrieval models. Recently, Irwin et al. (2020) and Feng et al. (2020) explored an extension of the retrieval method beyond 1D modeling since close-in exoplanets are subject to tidal locking and thus significant horizontal and latitudinal variations in the atmospheric properties, which can be explored by phase curve observations, are expected. The approach we have proposed in this study of including disequilibrium chemistry in spectral retrievals with a physical basis is also applicable to future 2D and 3D retrieval modeling, by adding horizontal or latitudinal transport term to the continuity-transport equation, Eq. (1) (e.g., Cooper & Showman 2006; Mendonça et al. 2018).

5. Conclusions

In this study, we have implemented the disequilibrium effect of vertical mixing or quenching to the spectral retrieval code ARCiS (Min et al. 2020) with a physical basis. Adopting a chemical relaxation method with a chemical timescale derived by Tsai et al. (2018), we have developed a module to compute the profiles of molecular abundances taking the disequilibrium effect into account for the major species in hydrogen/helium-dominated atmospheres, namely CH_4 , CO , H_2O , NH_3 , N_2 , and CO_2 . Then using ARCiS updated with this module, we have performed retrievals of the observed transmission spectra of 16 exoplanets with sizes ranging from Jupiter to mini-Neptune.

We have found indicative evidence of disequilibrium chemistry for HD 209458b and WASP-39b. For HD 209458b, the retrieved value of the eddy diffusion coefficient, which is used in the chemistry calculation, is as large as $\log_{10}(K_{zz}^{\text{Ch}} [\text{cm}^2 \text{s}^{-1}]) = 13.12^{+1.39}_{-4.61}$ from our standard disequilibrium retrieval, indicating that disequilibrium chemistry plays a significant role in determining the molecular abundance profiles in its atmosphere. Owing to the enhanced abundance of NH_3 due to the quenching effect, its retrieved spectrum exhibits a strong NH_3 absorption feature at $10.5 \mu\text{m}$, which is absent in the retrieved spectrum from the equilibrium retrieval. This feature is accessible by JWST/MIRI. Thus, HD 209458b offers a unique opportunity to study disequilibrium chemistry in exoplanet atmospheres. More-

over, for HAT-P-11b and GJ 436b, we obtained relatively different results between the disequilibrium and equilibrium retrievals such as a 2.9σ difference for the C/O ratio. This demonstrates the importance of taking disequilibrium chemistry into account for spectral retrieval, where we might otherwise misinterpret results. We have also examined the trend of the retrieved eddy diffusion coefficients over the equilibrium temperature, though no trend was found, possibly due to the limits of the current observational precision. This study makes clear that including a consideration of disequilibrium chemistry in spectral retrieval is essential in the coming era of JWST and Ariel.

Acknowledgements. We wish to thank S.-M. Tsai for kindly providing his calculation data for the code validation. The insightful advice and valuable comments on the manuscript received from K. Ohno are greatly appreciated. Also, we are grateful to P. Woitke, C. Visscher, and J. Moses for their helpful comments. Finally, we wish to thank the anonymous referee for his/her careful reading and constructive comments and the editor E. Lellouch for his helpful comments, both of which significantly helped improve this paper. The numerical computations were carried out on the PC cluster at the Center for Computational Astrophysics, National Astronomical Observatory of Japan. This work was supported by JSPS KAKENHI Grant Numbers JP21K13984 and JP21J04998. Y.K. acknowledges support from the European Union's Horizon 2020 Research and Innovation Programme under Grant Agreement 776403 and Special Postdoctoral Researcher Program at RIKEN. This work has made use of Numpy (Harris et al. 2020), Matplotlib (Hunter 2007), and corner.py (Foreman-Mackey 2016), and we are grateful to the developers of those packages.

References

- Agúndez, M., Parmentier, V., Venot, O., Hersant, F., & Selsis, F. 2014, *A&A*, 564, A73
- Agúndez, M., Venot, O., Iro, N., et al. 2012, *A&A*, 548, A73
- Allen, M., Yung, Y. L., & Waters, J. W. 1981, *J. Geophys. Res.*, 86, 3617
- Asplund, M., Amarsi, A. M., & Grevesse, N. 2021, arXiv e-prints, arXiv:2105.01661
- Baxter, C., Désert, J.-M., Tsai, S.-M., et al. 2021, *A&A*, 648, A127
- Benneke, B., Knutson, H. A., Lothringer, J., et al. 2019, *Nature Astronomy*, 3, 813
- Benneke, B. & Seager, S. 2012, *ApJ*, 753, 100
- Burcat, A., Ruscic, B., Chemistry, & of Tech., T. I. I. 2005
- Carter, A. L., Nikolov, N., Sing, D. K., et al. 2020, *MNRAS*, 494, 5449
- Chachan, Y., Knutson, H. A., Gao, P., et al. 2019, *AJ*, 158, 244
- Changeat, Q., Edwards, B., Waldmann, I. P., & Tinetti, G. 2019, *ApJ*, 886, 39
- Chubb, K. L., Rocchetto, M., Yurchenko, S. N., et al. 2021, *A&A*, 646, A21
- Cooper, C. S. & Showman, A. P. 2006, *ApJ*, 649, 1048
- Crossfield, I. J. M. & Kreidberg, L. 2017, *AJ*, 154, 261
- Drummond, B., Hébrard, E., Mayne, N. J., et al. 2020, *A&A*, 636, A68
- Drummond, B., Mayne, N. J., Manners, J., et al. 2018a, *ApJ*, 869, 28
- Drummond, B., Mayne, N. J., Manners, J., et al. 2018b, *ApJ*, 855, L31
- Eistrup, C., Walsh, C., & van Dishoeck, E. F. 2016, *A&A*, 595, A83
- Eistrup, C., Walsh, C., & van Dishoeck, E. F. 2018, *A&A*, 613, A14
- Feng, Y. K., Line, M. R., & Fortney, J. J. 2020, *AJ*, 160, 137
- Fischer, P. D., Knutson, H. A., Sing, D. K., et al. 2016, *ApJ*, 827, 19
- Fisher, C. & Heng, K. 2018, *MNRAS*, 481, 4698
- Foreman-Mackey, D. 2016, *The Journal of Open Source Software*, 1, 24
- Fraine, J. D., Deming, D., Gillon, M., et al. 2013, *ApJ*, 765, 127
- Gao, P. & Benneke, B. 2018, *ApJ*, 863, 165
- Gao, P., Marley, M. S., Zahnle, K., Robinson, T. D., & Lewis, N. K. 2017, *AJ*, 153, 139
- Gao, P., Thorngren, D. P., Lee, G. K. H., et al. 2020, *Nature Astronomy*, 4, 951
- Gardner, J. P., Mather, J. C., Clampin, M., et al. 2006, *Space Sci. Rev.*, 123, 485
- Giacobbe, P., Brogi, M., Gandhi, S., et al. 2021, *Nature*, 592, 205
- Grassi, T., Bovino, S., Schleicher, D. R. G., et al. 2014, *MNRAS*, 439, 2386
- Guillot, T. 2010, *A&A*, 520, A27
- Guo, X., Crossfield, I. J. M., Dragomir, D., et al. 2020, *AJ*, 159, 239
- Harris, C. R., Millman, K. J., van der Walt, S. J., et al. 2020, *Nature*, 585, 357
- Hu, R., Seager, S., & Bains, W. 2012, *ApJ*, 761, 166
- Hu, R., Seager, S., & Bains, W. 2013, *ApJ*, 769, 6
- Huitson, C. M., Sing, D. K., Pont, F., et al. 2013, *MNRAS*, 434, 3252
- Hunter, J. D. 2007, *Computing in Science & Engineering*, 9, 90
- Irwin, P. G. J., Parmentier, V., Taylor, J., et al. 2020, *MNRAS*, 493, 106
- Irwin, P. G. J., Teanby, N. A., de Kok, R., et al. 2008, *J. Quant. Spectr. Rad. Transf.*, 109, 1136
- Kasting, J. F., Holland, H. D., & Pinto, J. P. 1985, *J. Geophys. Res.*, 90, 10,497
- Kawashima, Y. & Ikoma, M. 2018, *ApJ*, 853, 7

- Kawashima, Y. & Ikoma, M. 2019, *ApJ*, 877, 109
- Knutson, H. A., Benneke, B., Deming, D., & Homeier, D. 2014, *Nature*, 505, 66
- Knutson, H. A., Madhusudhan, N., Cowan, N. B., et al. 2011, *ApJ*, 735, 27
- Komacek, T. D., Showman, A. P., & Parmentier, V. 2019, *ApJ*, 881, 152
- Kreidberg, L., Bean, J. L., Désert, J.-M., et al. 2014, *Nature*, 505, 69
- Kreidberg, L., Line, M. R., Bean, J. L., et al. 2015, *ApJ*, 814, 66
- Lavvas, P. & Koskinen, T. 2017, *ApJ*, 847, 32
- Liang, M.-C., Parkinson, C. D., Lee, A. Y. T., Yung, Y. L., & Seager, S. 2003, *ApJ*, 596, L247
- Line, M. R., Knutson, H., Wolf, A. S., & Yung, Y. L. 2014, *ApJ*, 783, 70
- Line, M. R., Wolf, A. S., Zhang, X., et al. 2013, *ApJ*, 775, 137
- Lothringer, J. D., Benneke, B., Crossfield, I. J. M., et al. 2018, *AJ*, 155, 66
- MacDonald, R. J. & Madhusudhan, N. 2017, *MNRAS*, 469, 1979
- Mayor, M. & Queloz, D. 1995, *Nature*, 378, 355
- McCullough, P. R., Crouzet, N., Deming, D., & Madhusudhan, N. 2014, *ApJ*, 791, 55
- Mendonça, J. M., Tsai, S.-m., Malik, M., Grimm, S. L., & Heng, K. 2018, *ApJ*, 869, 107
- Miller-Ricci Kempton, E., Zahnle, K., & Fortney, J. J. 2012, *ApJ*, 745, 3
- Min, M., Ormel, C. W., Chubb, K., Helling, C., & Kawashima, Y. 2020, *A&A*, 642, A28
- Mollière, P., Stolker, T., Lacour, S., et al. 2020, *A&A*, 640, A131
- Mollière, P., Wardenier, J. P., van Boekel, R., et al. 2019, *A&A*, 627, A67
- Mordasini, C., van Boekel, R., Mollière, P., Henning, T., & Benneke, B. 2016, *ApJ*, 832, 41
- Morello, G., Waldmann, I. P., Tinetti, G., et al. 2015, *ApJ*, 802, 117
- Morley, C. V., Fortney, J. J., Kempton, E. M.-R., et al. 2013, *ApJ*, 775, 33
- Morley, C. V., Fortney, J. J., Marley, M. S., et al. 2015, *ApJ*, 815, 110
- Morley, C. V., Knutson, H., Line, M., et al. 2017, *AJ*, 153, 86
- Moses, J. I. 2014, *Philosophical Transactions of the Royal Society of London Series A*, 372, 20130073
- Moses, J. I., Fouchet, T., Bézard, B., et al. 2005, *Journal of Geophysical Research (Planets)*, 110, E08001
- Moses, J. I., Visscher, C., Fortney, J. J., et al. 2011, *ApJ*, 737, 15
- Nikolov, N., Sing, D. K., Fortney, J. J., et al. 2018, *Nature*, 557, 526
- Nikolov, N., Sing, D. K., Pont, F., et al. 2014, *MNRAS*, 437, 46
- Notsu, S., Eistrup, C., Walsh, C., & Nomura, H. 2020, *MNRAS*, 499, 2229
- Öberg, K. I., Murray-Clay, R., & Bergin, E. A. 2011, *ApJ*, 743, L16
- Ohno, K. & Kawashima, Y. 2020, *ApJ*, 895, L47
- Ormel, C. W. & Min, M. 2019, *A&A*, 622, A121
- Oshagh, M., Bauer, F. F., Lafarga, M., et al. 2020, *A&A*, 643, A64
- Oshagh, M., Santos, N. C., Ehrenreich, D., et al. 2014, *A&A*, 568, A99
- Parmentier, V., Showman, A. P., & Lian, Y. 2013, *A&A*, 558, A91
- Pont, F., Sing, D. K., Gibson, N. P., et al. 2013, *MNRAS*, 432, 2917
- Prinn, R. G. & Barshay, S. S. 1977, *Science*, 198, 1031
- Rimmer, P. B. & Helling, C. 2016, *ApJS*, 224, 9
- Sing, D. K., Fortney, J. J., Nikolov, N., et al. 2016, *Nature*, 529, 59
- Sing, D. K., Lecavelier des Etangs, A., Fortney, J. J., et al. 2013, *MNRAS*, 436, 2956
- Sing, D. K., Wakeford, H. R., Showman, A. P., et al. 2015, *MNRAS*, 446, 2428
- Smith, M. D. 1998, *Icarus*, 132, 176
- Thorngren, D., Gao, P., & Fortney, J. J. 2019, *ApJ*, 884, L6
- Thorngren, D. P. & Fortney, J. J. 2018, *AJ*, 155, 214
- Tinetti, G., Drossart, P., Eccleston, P., et al. 2018, *Experimental Astronomy*, 46, 135
- Trotta, R. 2008, *Contemporary Physics*, 49, 71
- Tsai, S.-M., Kitzmann, D., Lyons, J. R., et al. 2018, *ApJ*, 862, 31
- Tsai, S.-M., Lyons, J. R., Grosheintz, L., et al. 2017, *ApJS*, 228, 20
- Venot, O., Hébrard, E., Agúndez, M., et al. 2012, *A&A*, 546, A43
- Visscher, C., Moses, J. I., & Saslow, S. A. 2010, *Icarus*, 209, 602
- Wakeford, H. R., Sing, D. K., Deming, D., et al. 2013, *MNRAS*, 435, 3481
- Wakeford, H. R., Sing, D. K., Deming, D., et al. 2018, *AJ*, 155, 29
- Wakeford, H. R., Sing, D. K., Kataria, T., et al. 2017, *Science*, 356, 628
- Waldmann, I. P., Tinetti, G., Rocchetto, M., et al. 2015, *ApJ*, 802, 107
- Welbanks, L., Madhusudhan, N., Allard, N. F., et al. 2019, *ApJ*, 887, L20
- Woitke, P., Helling, C., Hunter, G. H., et al. 2018, *A&A*, 614, A1
- Wong, I., Benneke, B., Gao, P., et al. 2020, *AJ*, 159, 234
- Yung, Y. L., Drew, W. A., Pinto, J. P., & Friedl, R. R. 1988, *Icarus*, 73, 516
- Zahnle, K., Marley, M. S., & Fortney, J. J. 2009, *arXiv e-prints*, arXiv:0911.0728
- Zahnle, K., Marley, M. S., Morley, C. V., & Moses, J. I. 2016, *ApJ*, 824, 137
- Zahnle, K. J. & Marley, M. S. 2014, *ApJ*, 797, 41
- Zhang, X. & Showman, A. P. 2018, *ApJ*, 866, 1

Appendix A: Atmospheric Profiles

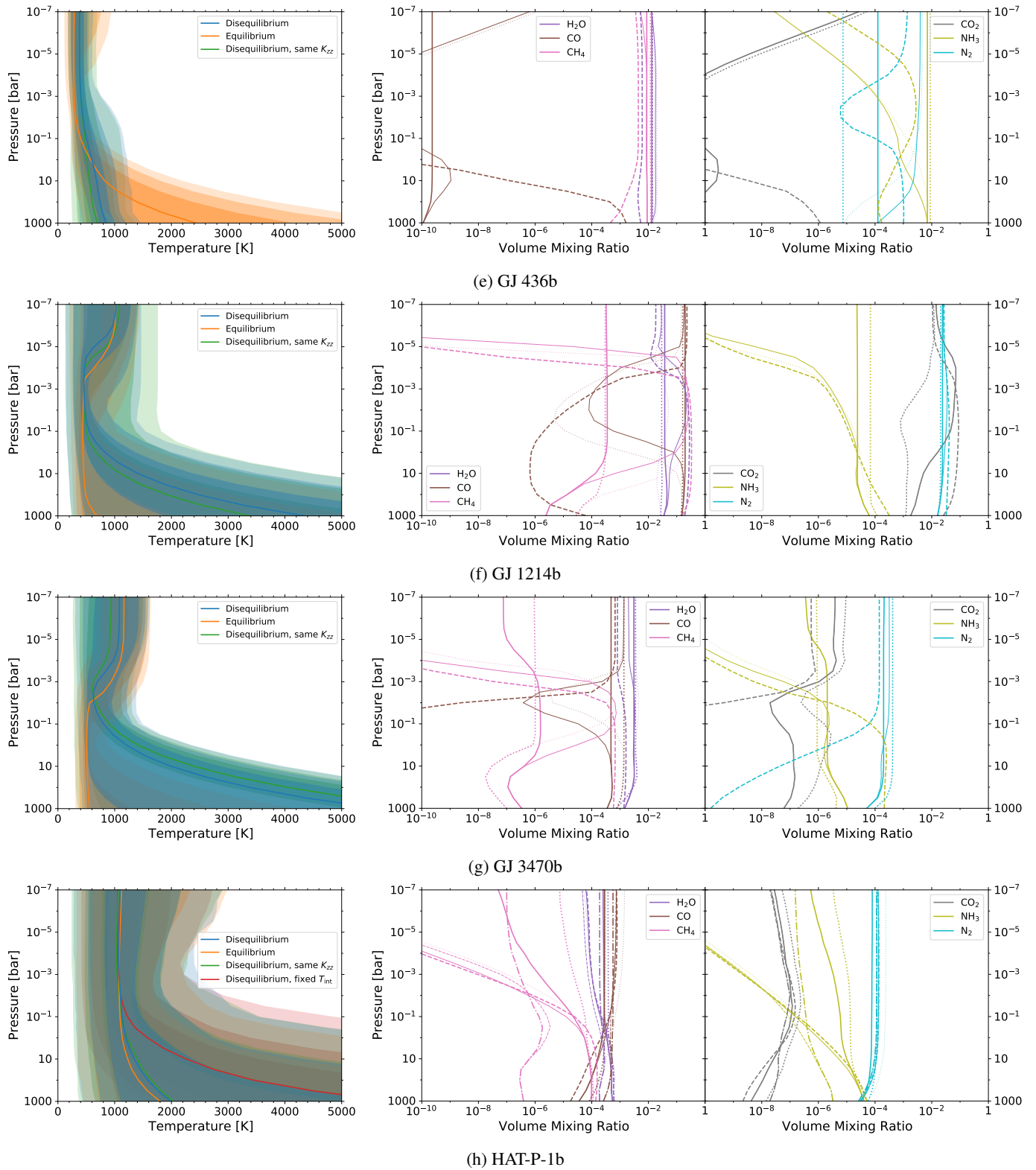
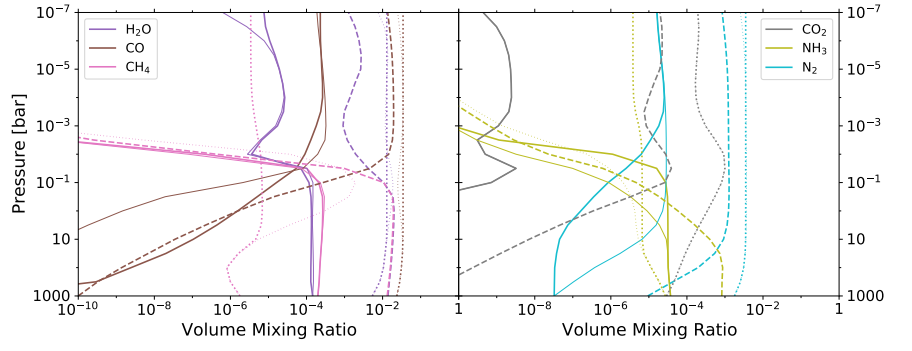
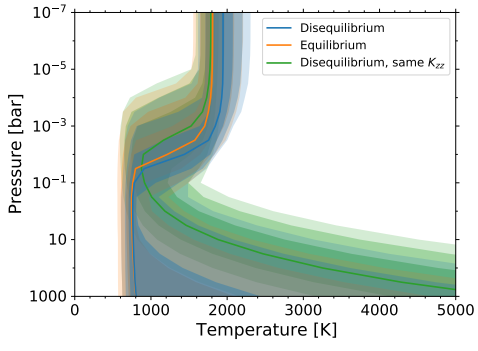
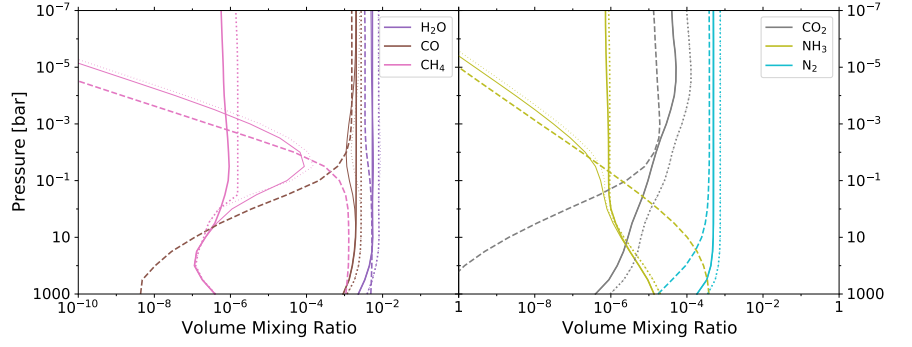
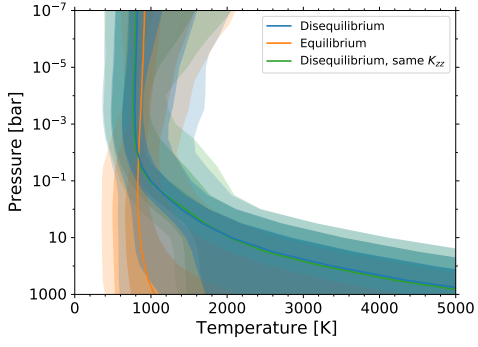


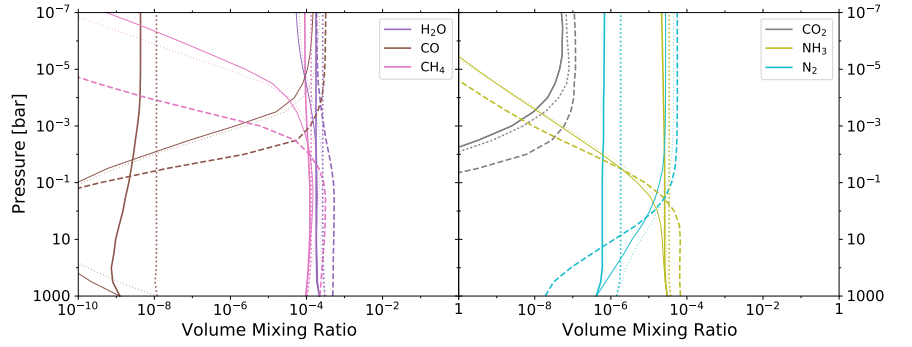
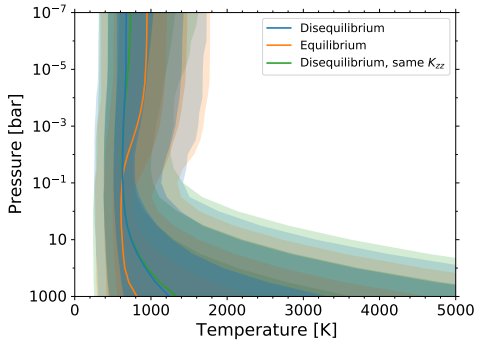
Fig. A.1: As for Fig. 2 for the remaining planets.



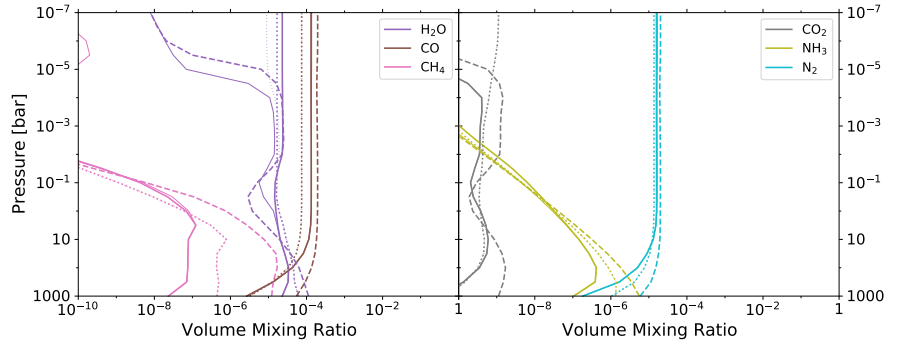
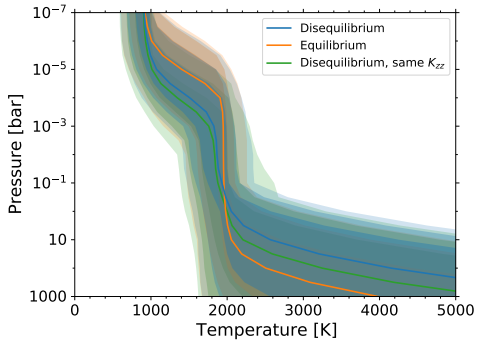
(i) HAT-P-12b



(j) HAT-P-26b



(k) HD 97658b



(l) WASP-6b

Fig. A.1: Continued.

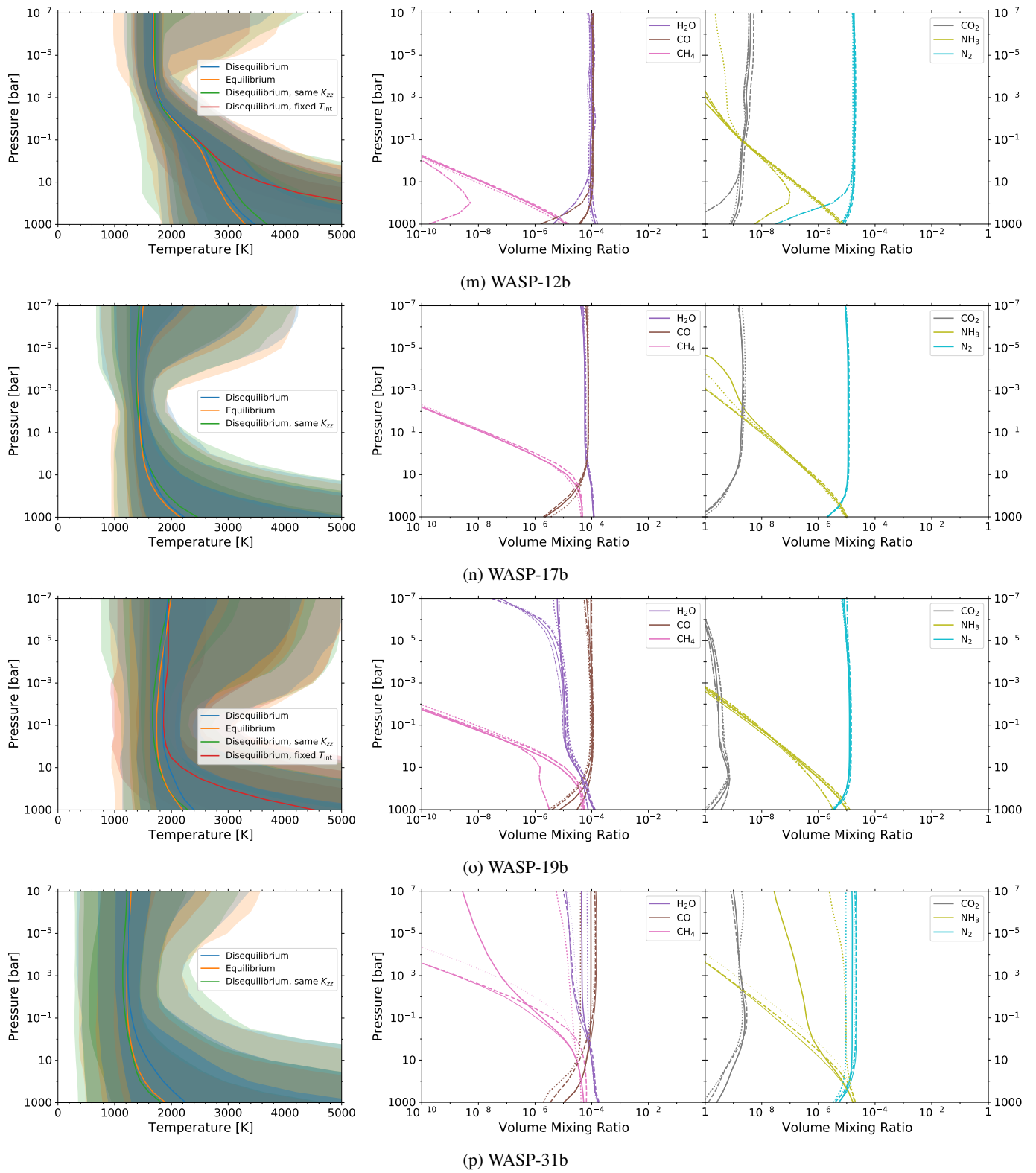


Fig. A.1: Continued.

Appendix B: Corner Plots

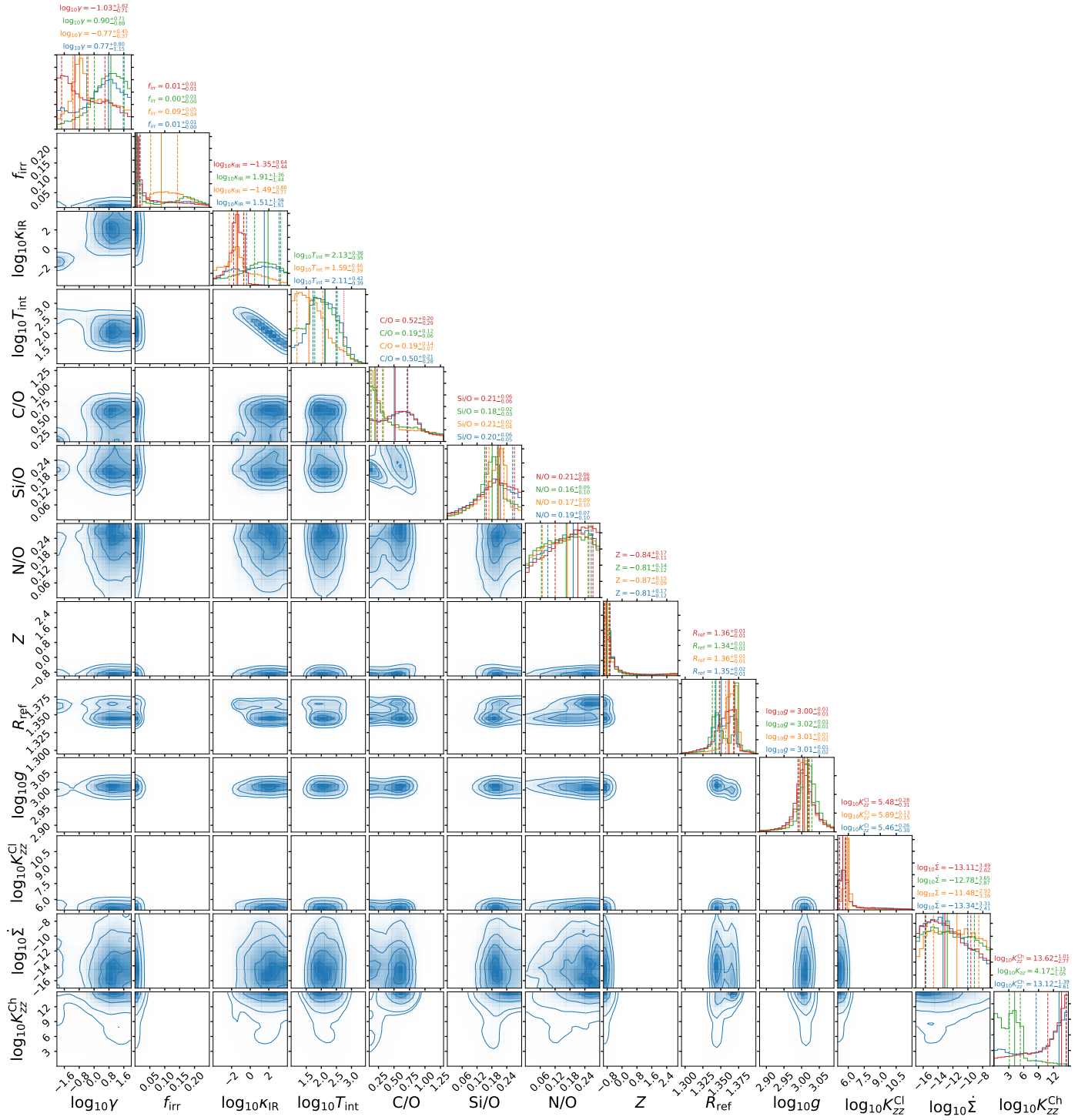


Fig. B.1: Corner plots for the standard disequilibrium retrieval (blue). Also shown in the posterior probability distribution plots are the results of the equilibrium retrieval (orange) and disequilibrium retrievals with the same K_{zz} (green) and with fixed T_{int} (red; only shown for planets with masses larger than half Jupiter mass). The vertical solid and dashed lines in the posterior plots indicate the median value and the 1σ confidence interval for each parameter, respectively. K_{zz} retrieved from the same- K_{zz} retrieval is shown in the place of K_{zz}^{Ch} , and the vertical red dotted line in the posterior plot of $\log_{10} T_{\text{int}}$ is the value assumed in the T_{int} -fixed retrieval. The unit for each parameter is the same as that used in Table 2.

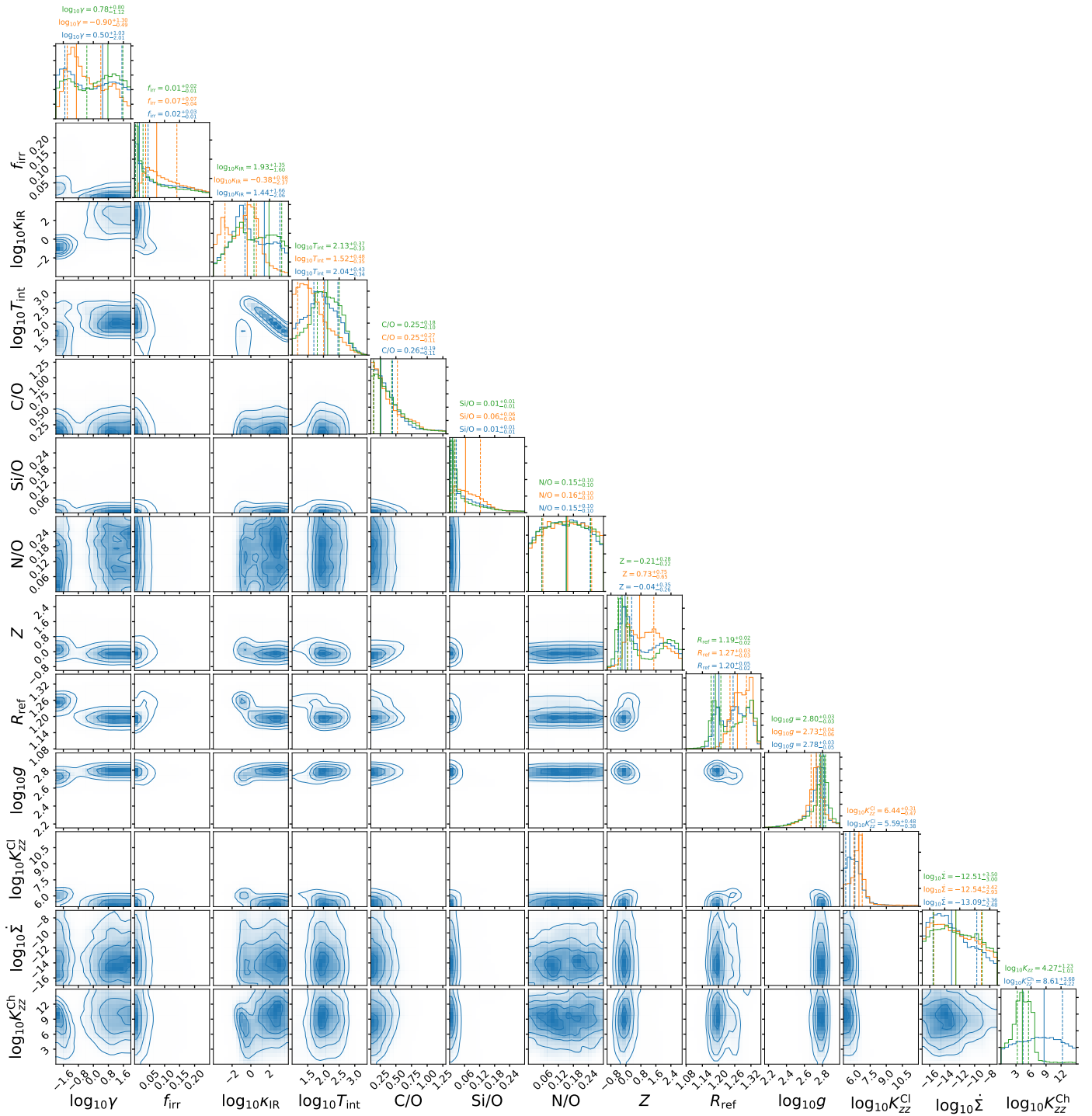
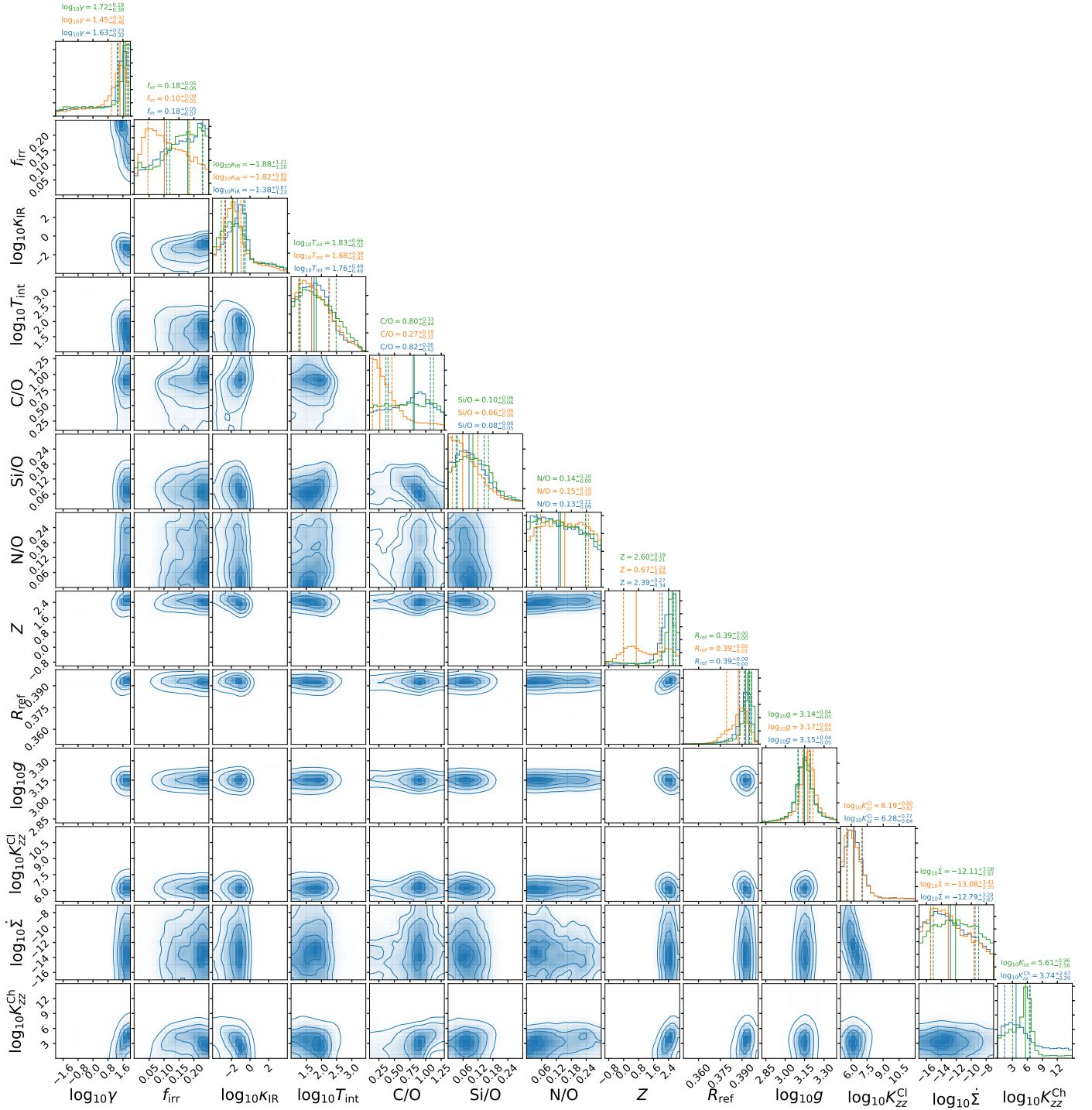
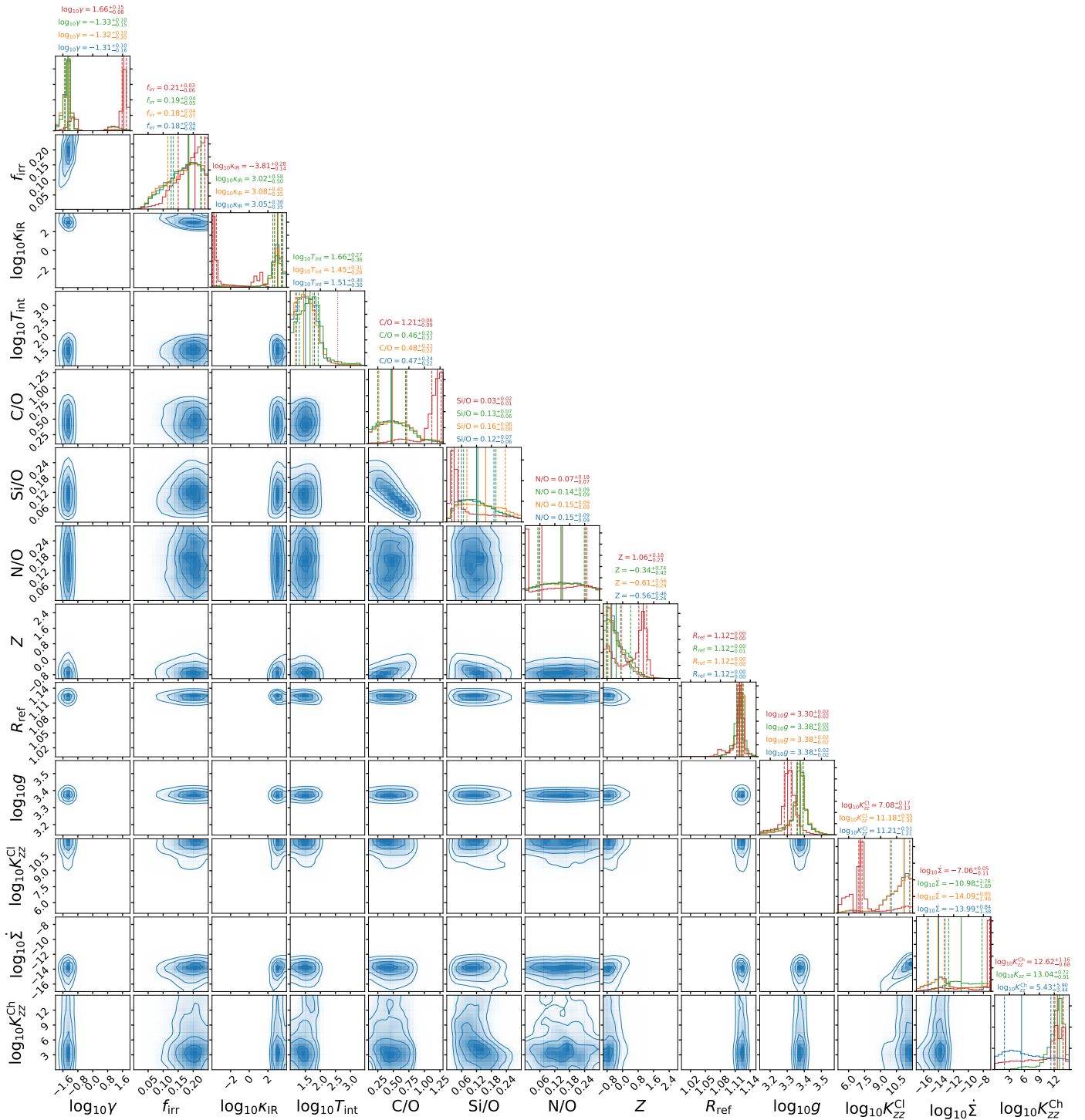


Fig. B.1: Continued



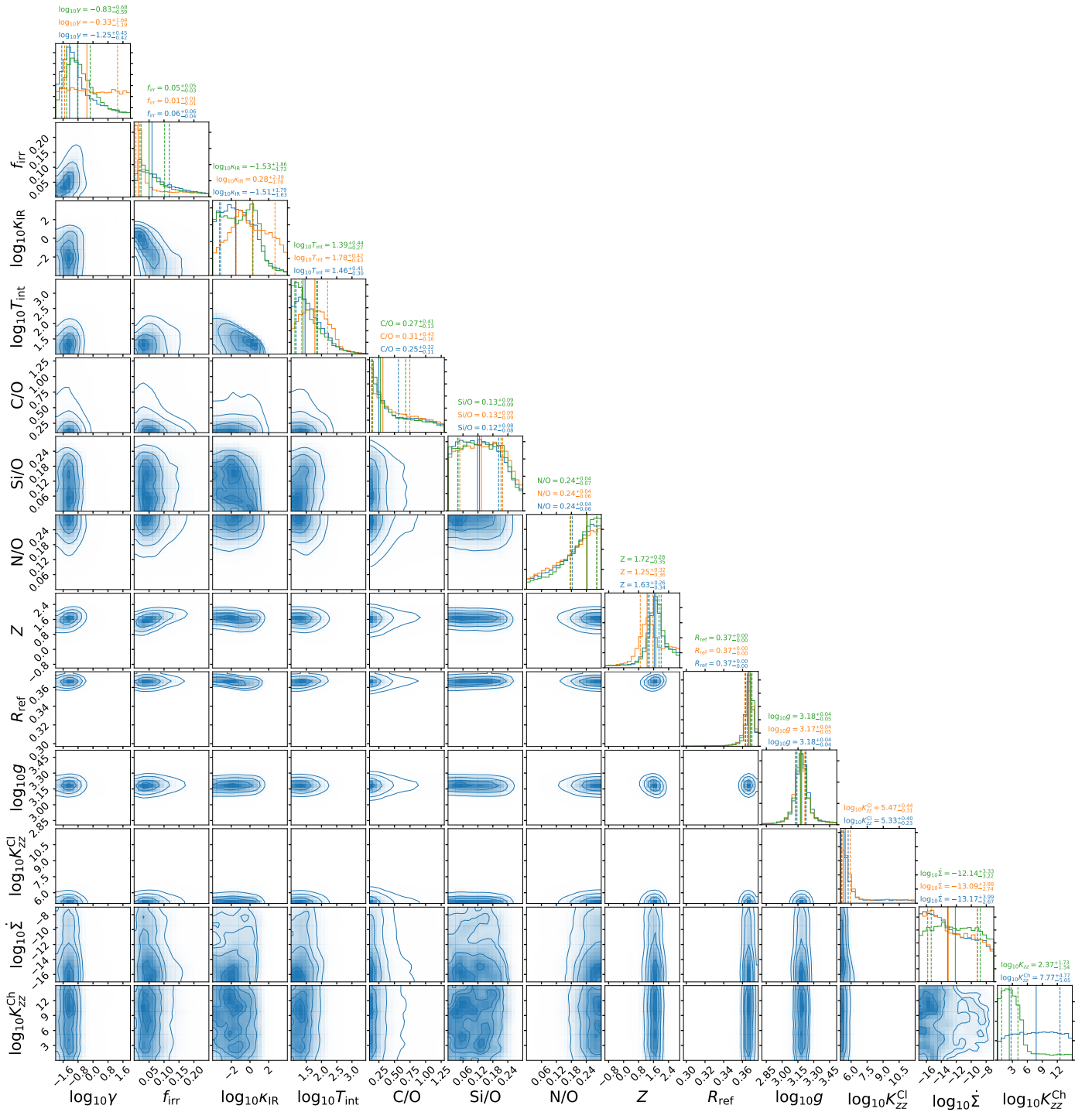
(c) HAT-P-11b

Fig. B.1: Continued



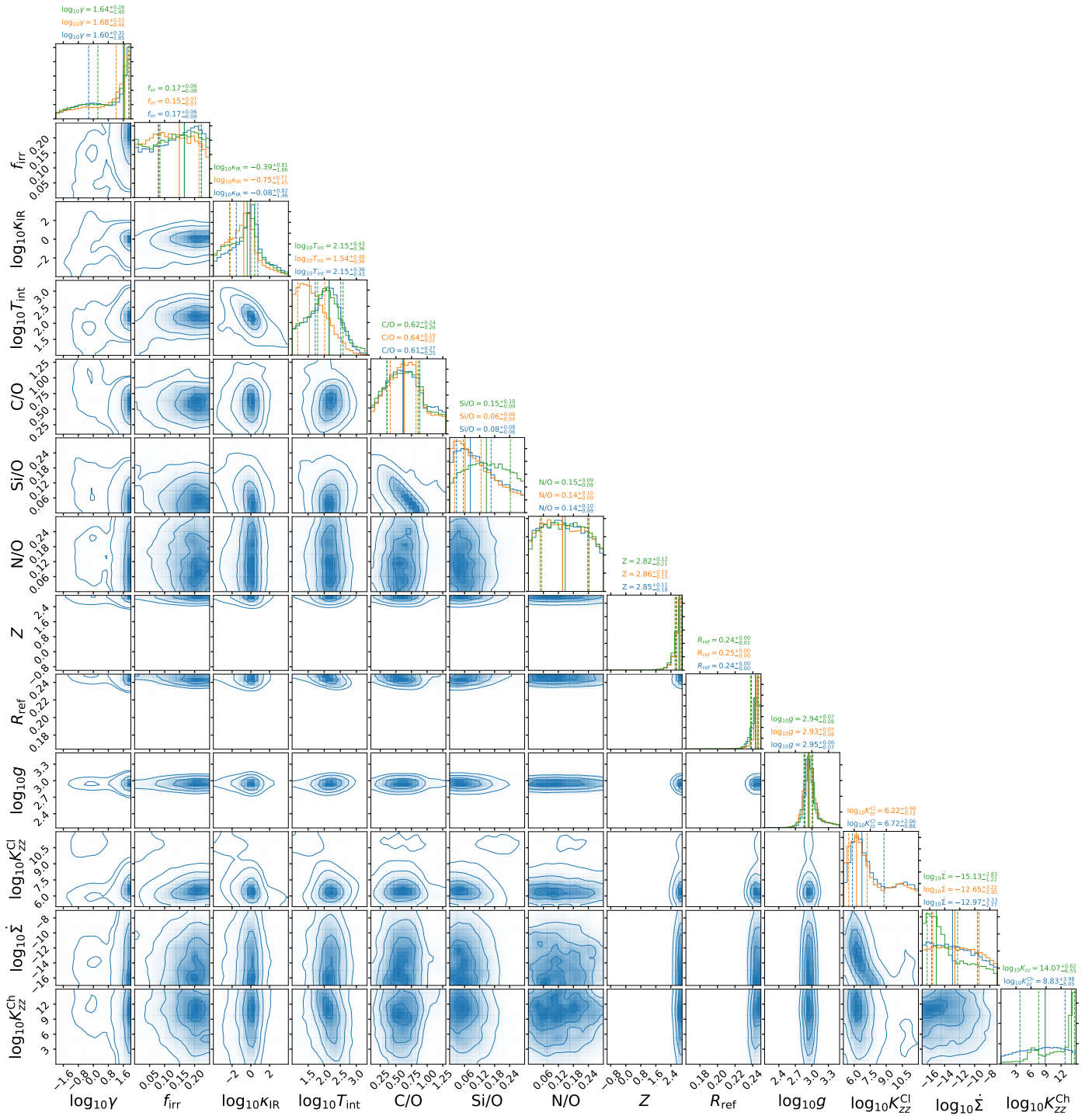
(d) HD 189733b

Fig. B.1: Continued



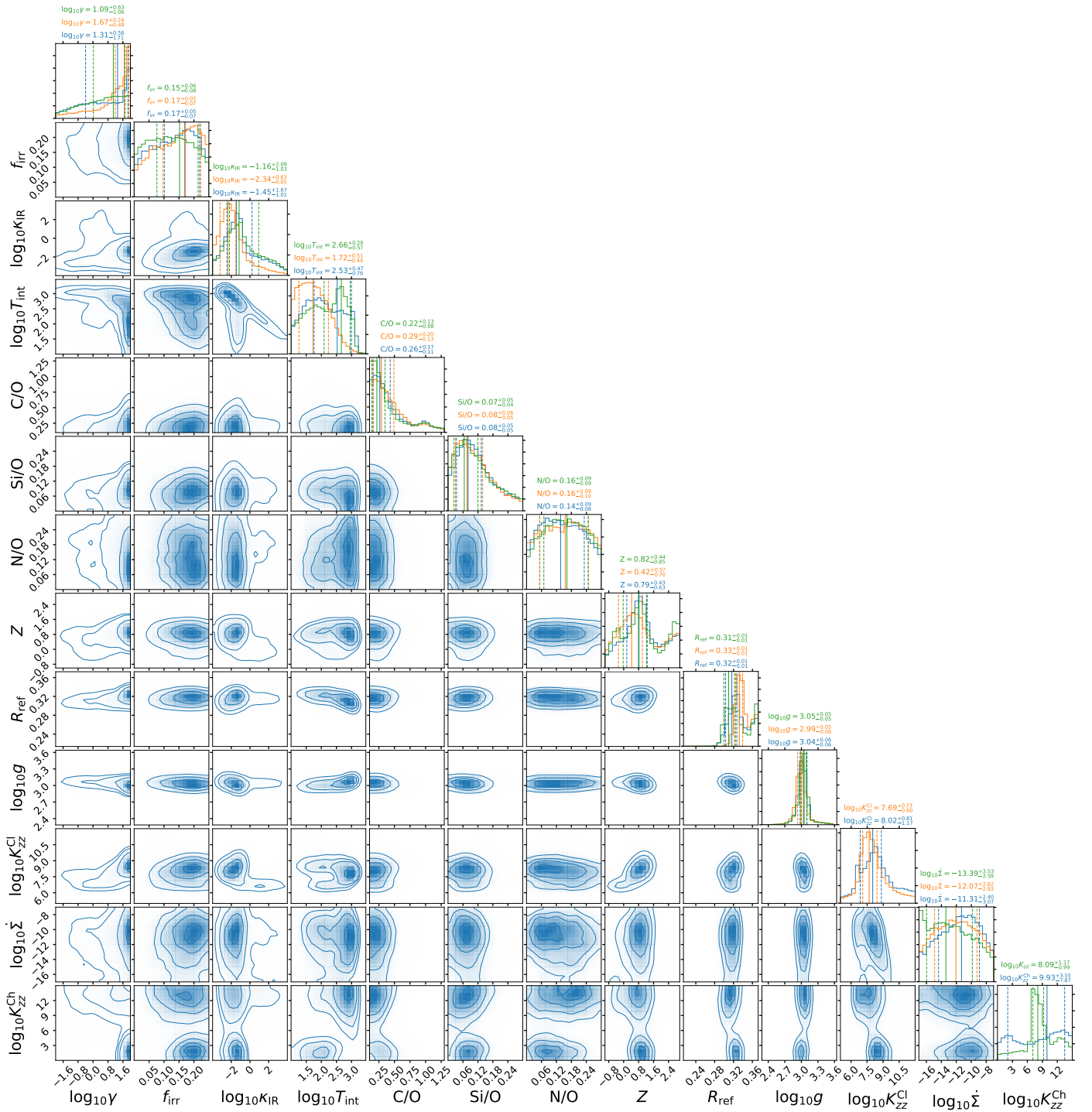
(e) GJ 436b

Fig. B.1: Continued



(f) GJ 1214b

Fig. B.1: Continued



(g) GJ 3470b

Fig. B.1: Continued

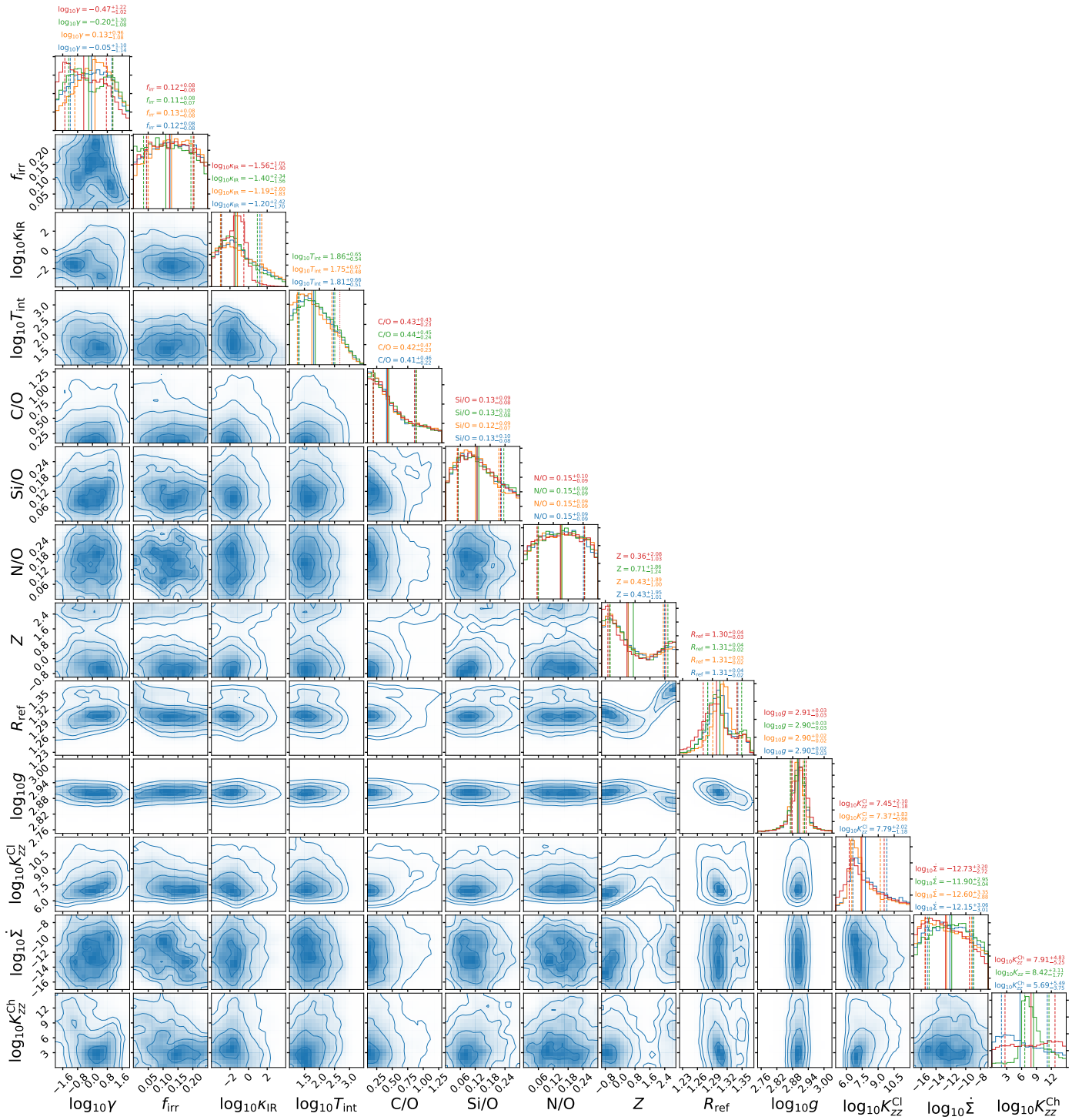
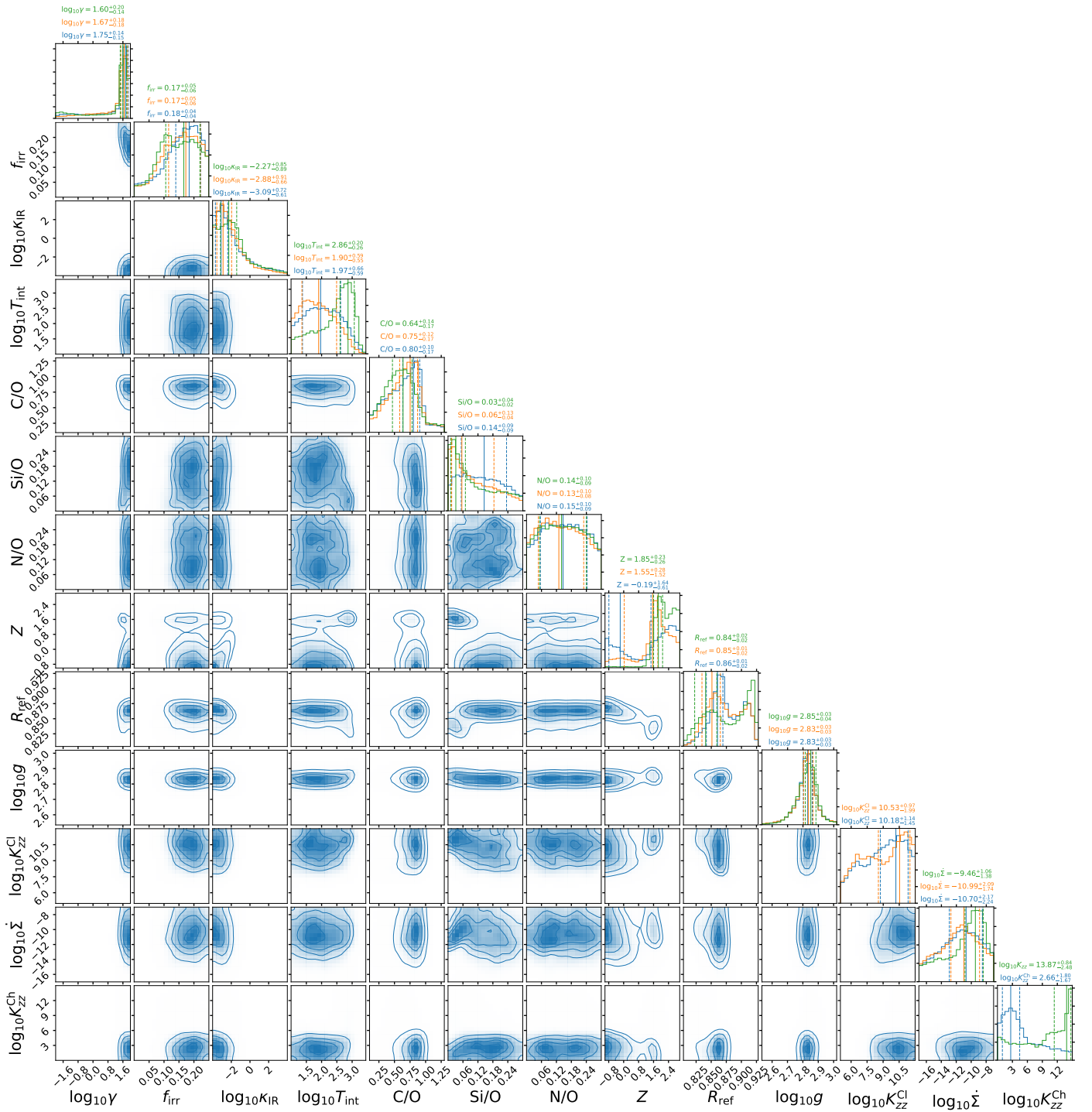
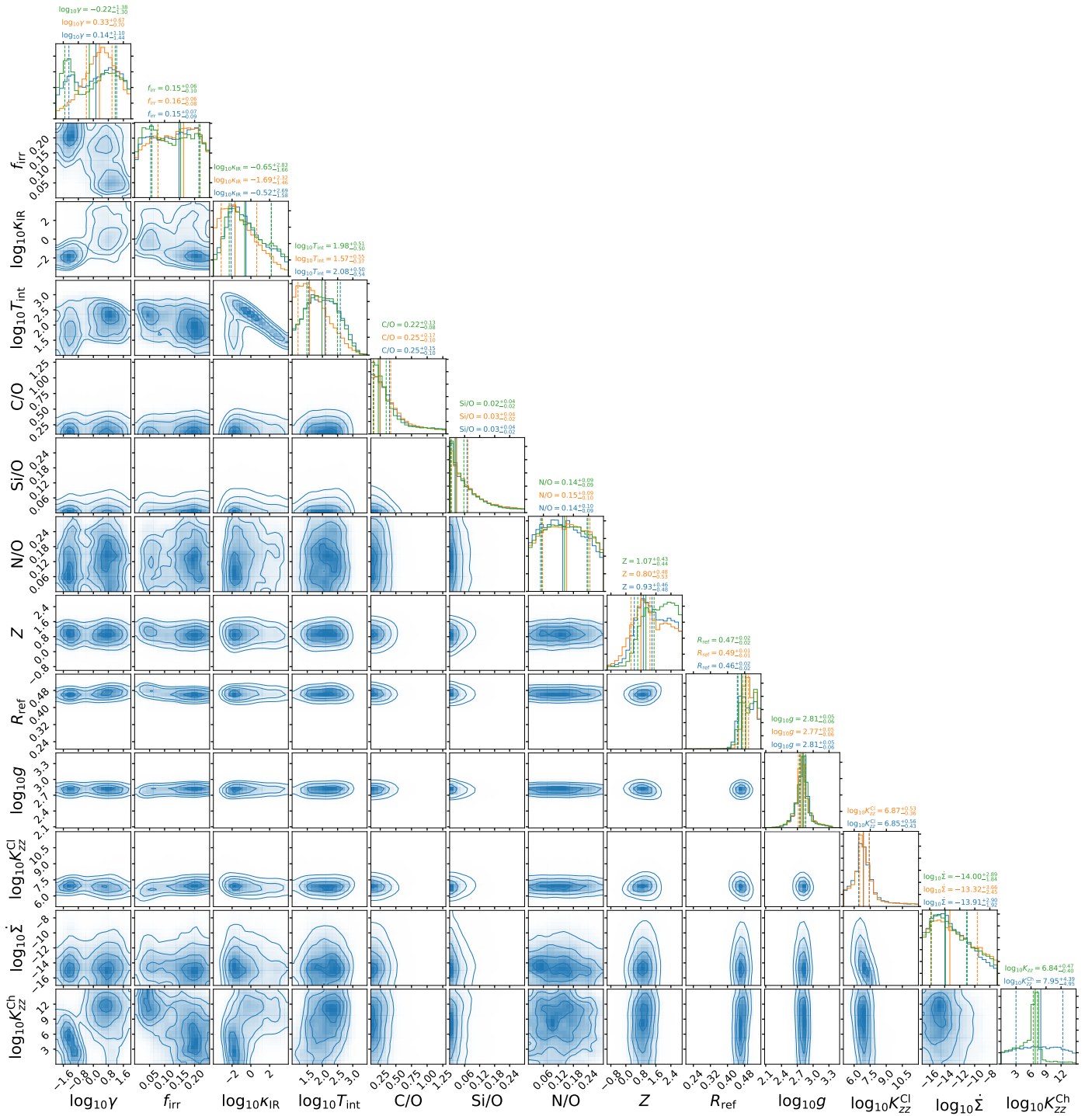


Fig. B.1: Continued



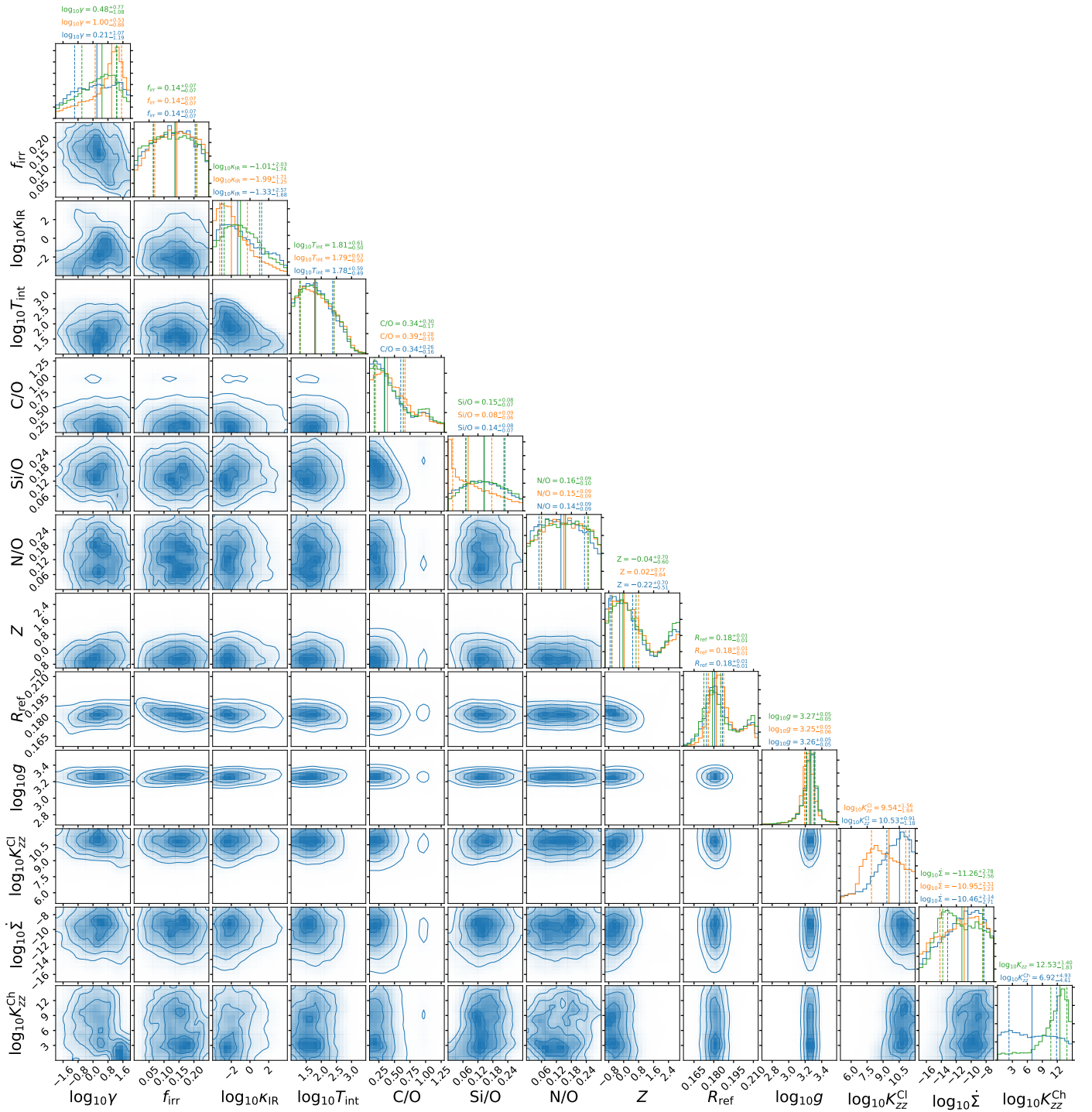
(i) HAT-P-12b

Fig. B.1: Continued



(j) HAT-P-26b

Fig. B.1: Continued



(k) HD 97658b

Fig. B.1: Continued

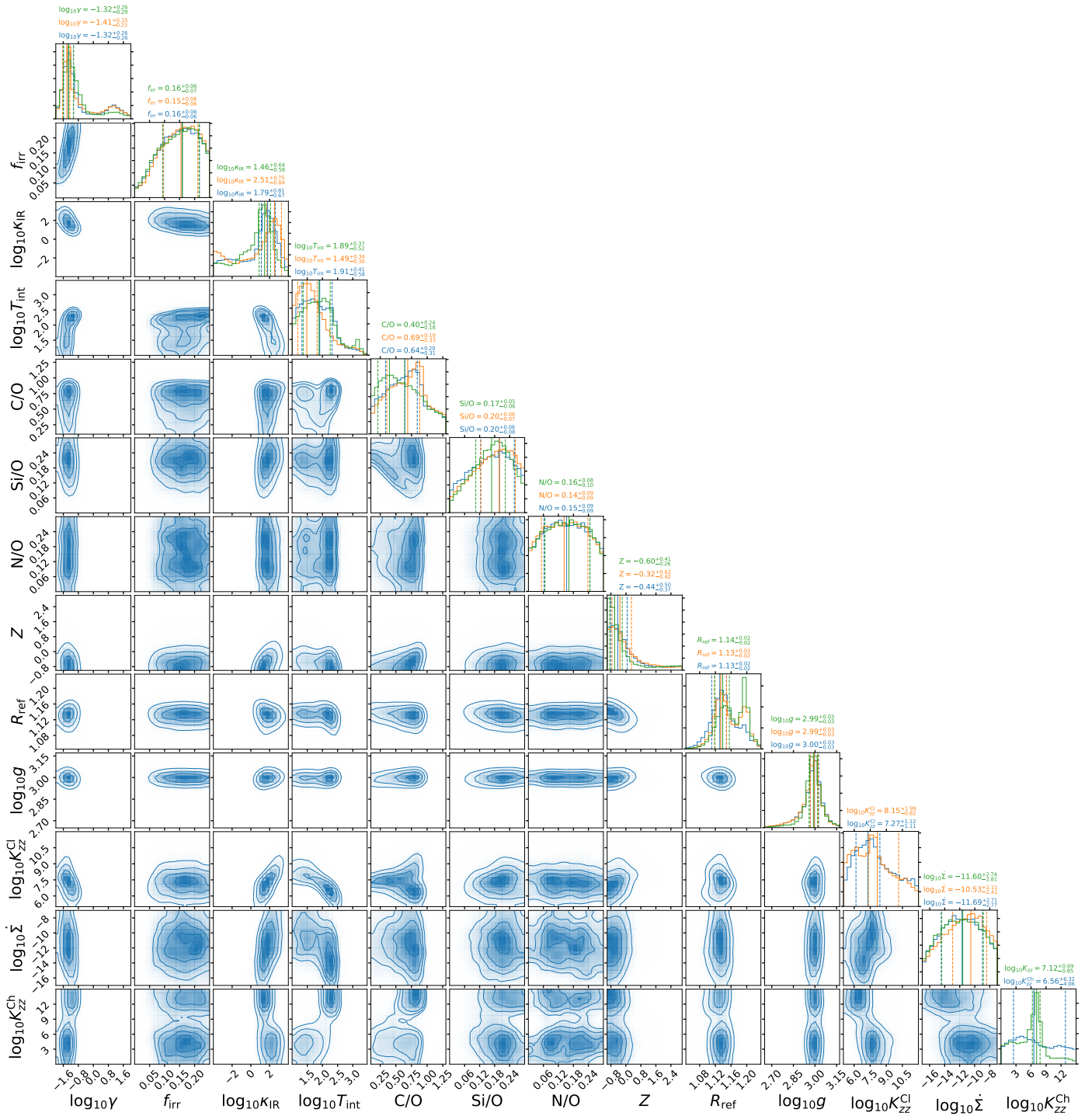
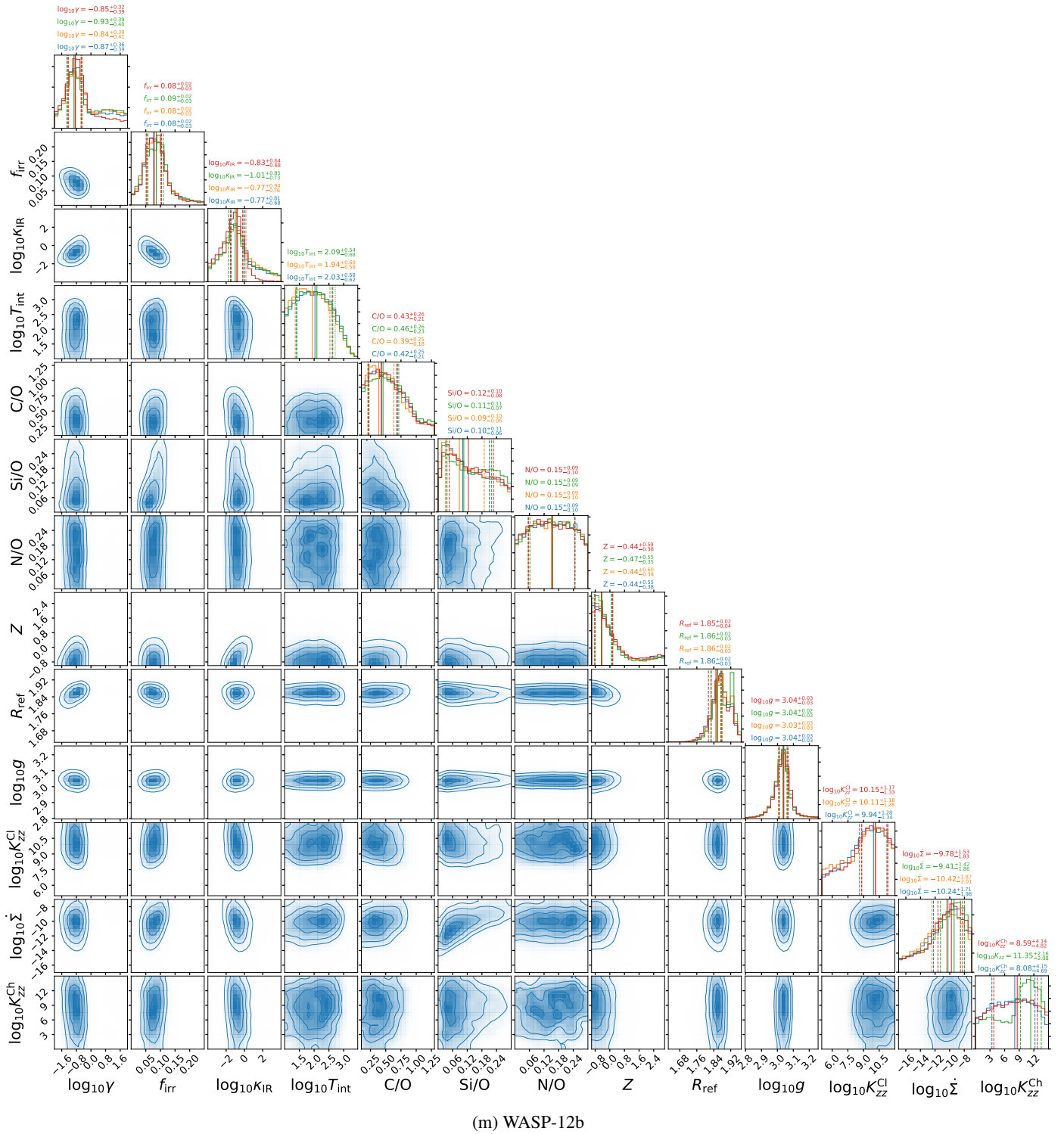
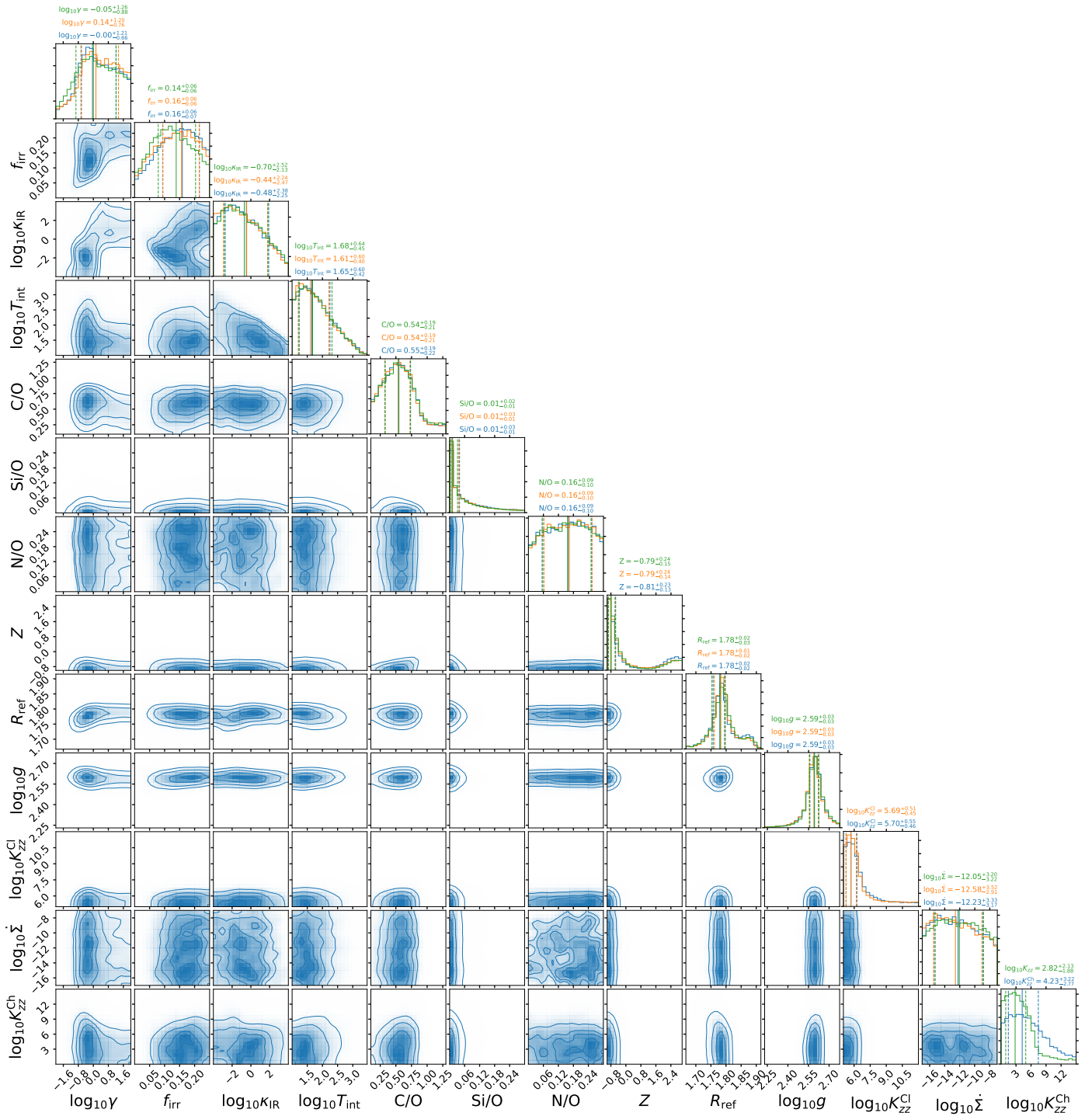


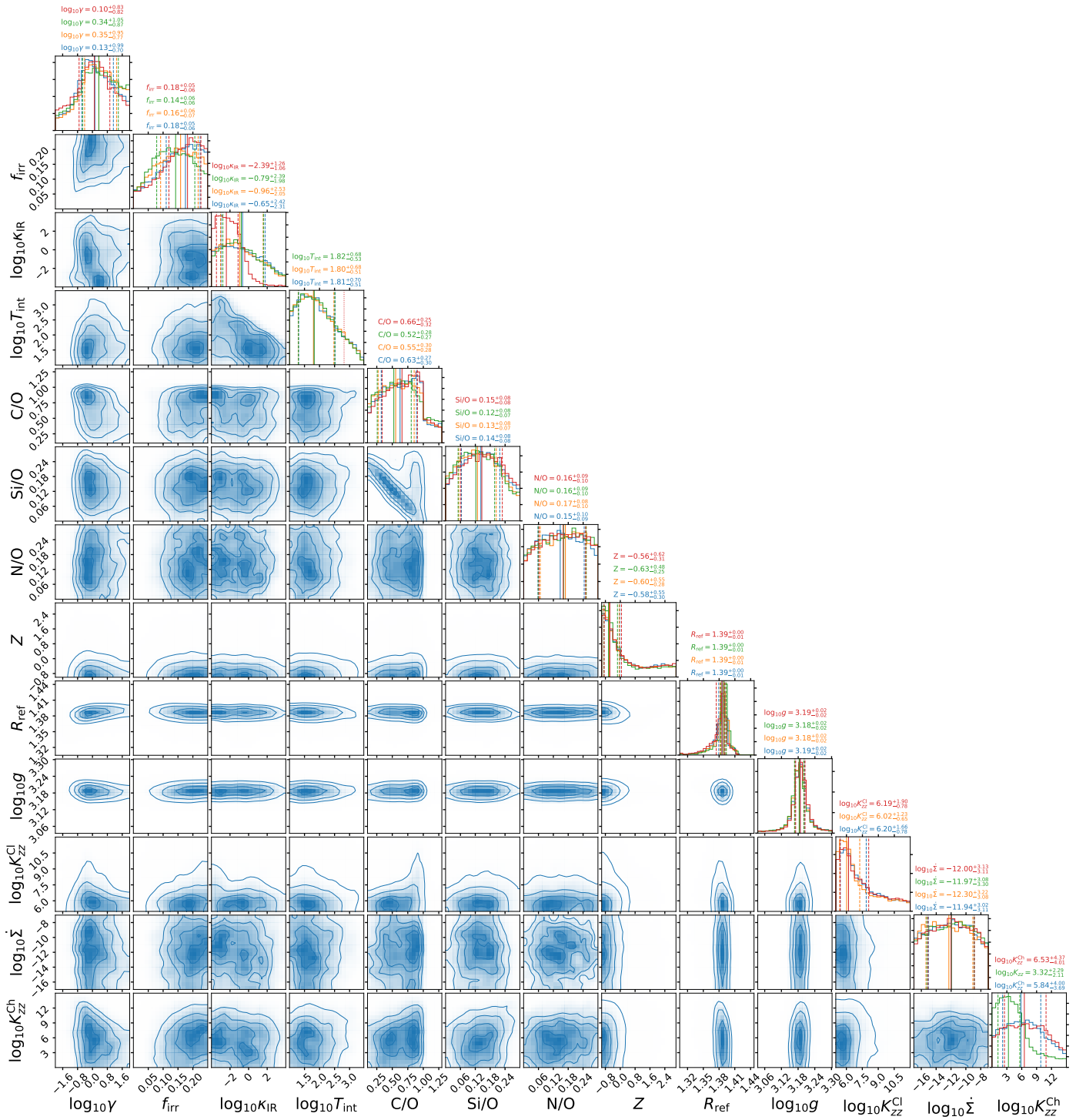
Fig. B.1: Continued





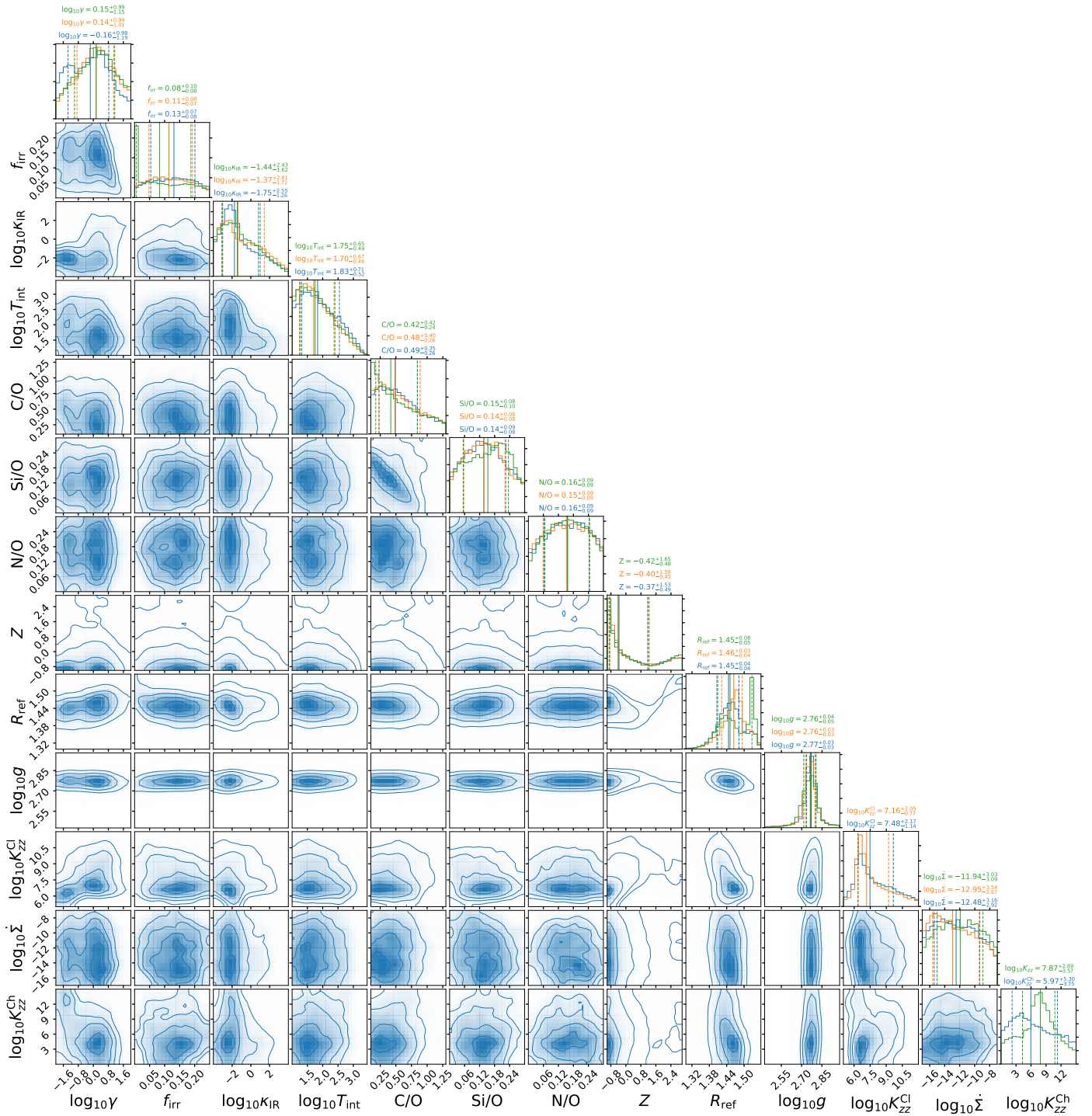
(n) WASP-17b

Fig. B.1: Continued



(o) WASP-19b

Fig. B.1: Continued



(p) WASP-31b

Fig. B.1: Continued